Pyroxenes as Tracers of Mantle Water Variations

Jessica M. Warren¹ and Erik H. Hauri²

¹Department of Geological & Environmental Sciences, Stanford University, 450 Serra Mall,

Building 320, Stanford CA 94305, USA. (warrenj@stanford.edu)

²Department of Terrestrial Magnetism, Carnegie Institution of Washington, 5241 Broad

Branch Road, NW, Washington, DC 20015, USA. (hauri@dtm.ciw.edu)

Submitted to Journal of Geophysical Research on April 30, 2013.

First revisions submitted to Journal of Geophysical Research on Nov 4, 2013.

Second revisions submitted to Journal of Geophysical Research on Feb 20, 2014.

ccepted

This article has been accepted for publication and undergone full peer review but has not been through the copyediting, typesetting, pagination and proofreading process which may lead to differences between this version and the Version of Record. Please cite this article as doi: 10.1002/2013JB010328

Abstract

The concentration and distribution of volatiles in the Earth's mantle influences properties such as melting temperature, conductivity, and viscosity. To constrain upper mantle water content, concentrations of H₂O, P, and F were measured in olivine, orthopyroxene and clinopyroxene by secondary ion mass spectrometry. Analyzed peridotites are xenoliths (Pali Aike, Spitsbergen, Samoa), orogenic peridotites (Josephine Peridotite), and abyssal peridotites (Gakkel Ridge, Southwest Indian Ridge, Tonga Trench). The comparison of fresh and altered peridotites demonstrates that low to moderate levels of alteration do not affect H₂O concentrations, in agreement with mineral diffusion data. Olivines have diffusively lost water during emplacement, as demonstrated by disequilibrium between olivine and co-existing pyroxenes. In contrast, clinopyroxene and orthopyroxene preserve their high temperature water contents, and their partitioning agrees with published experiments and other xenoliths. Hence, olivine water concentrations can be determined from pyroxene concentrations using mineral-mineral partition coefficients. Clinopyroxenes have 60-670 ppm H₂O, while orthopyroxenes have 10-300 ppm, which gives calculated olivine concentrations of 8-34 ppm. The highest olivine water concentration translates to an effective viscosity of 6×10¹⁹ Pa s at 1250°C and ~15 km depth, compared to a dry effective viscosity of 2.5×10²¹ Pa s. Bulk rock water concentrations, calculated using mineral modes, are 20-220 ppm and correlate with peridotite indices of melt depletion. However, trace element melt modeling indicates that peridotites have too much water relative to their rare earth element concentrations, which may be explained by late-stage melt addition, during which only hydrogen diffuses fast enough for re-equilibration.

Key points (80 character limit)

- 1: Peridotite pyroxenes provide constraints on upper mantle water variations.
- 2: Water in olivine is calculated from water in pyroxene and partition coefficients.
- 3: Peridotites are relatively water-rich for the residues of partial melting.

1. Introduction

The presence of water in the Earth's mantle affects many of its properties, from the depth of melting to the rheology of minerals. In the upper mantle, water is hosted in all the main mineral phases (olivine, orthopyroxene, clinopyroxene and garnet) of peridotite. These minerals are referred to as nominally anhydrous minerals (NAMs) as they do not contain hydrous groups in their formulas. Nonetheless, the presence of trace amounts of water reduces mantle viscosity by two to three orders of magnitude and results in the onset of melting tens of kilometers deeper than in dry mantle (Hirth & Kohlstedt, 1996). Water in olivine has also been shown to change the principle slip system for olivine during dislocation creep (Jung and Karato, 2001), the dominant mechanism by which flow in the uppermost mantle occurs.

Traditionally, analysis of water has been done by Fourier transform infrared spectroscopy (FTIR; e.g., Bell and Rossman, 1992). Analysis by FTIR requires oriented crystals with at least two polished surfaces (e.g., Bell et al., 2003), which is difficult for small grains. In addition, there has been much debate regarding the interpretation of OH stretching bands and the conversion of complex absorption spectra into water concentrations (e.g., Bell et al., 2003; Aubaud et al., 2009; Kovács et al., 2010; Stalder et al., 2012; Mosenfelder & Rossman, 2013a, 2013b; Withers, 2013).

Recently, analysis of NAMs using secondary ion mass spectrometry (SIMS) has become routine, due to technique development and availability of mineral standards (Koga et al., 2003; Hauri et al., 2006; Aubaud et al., 2007; Mosenfelder et al., 2011; Withers et al., 2012; Mosenfelder & Rossman, 2013a, 2013b). SIMS has the advantage over FTIR in that

the analysis is not dependent on mineral orientation and only one polished crystal surface is required. However, the detection limit for water by SIMS is generally higher than by FTIR, due to background water concentrations and detector sensitivity. Also, the majority of SIMS olivine standards have been calibrated by FTIR and thus are subject to the same uncertainties as FTIR data (Koga et al., 2003; Aubaud et al., 2007), though recent work has crosscalibrated olivine standards with other techniques (Aubaud et al., 2009; Mosenfelder et al., 2011; Withers et al., 2012). In contrast, orthopyroxene and clinopyroxene have higher water concentrations (Bell & Rossman, 1992; Ingrin & Skogby, 2000; Demouchy et al., 2006; Grant et al., 2006, 2007a, 2007b; Hauri et al., 2006; Kohn & Grant, 2006; Skogby, 2006; Withers & Hirschmann, 2007; Tenner et al., 2009, 2012; Peslier, 2010; Ardia et al., 2012) and less uncertainty exists with respect to pyroxene standard calibrations (Koga et al., 2003; Aubaud et al., 2007; Mosenfelder & Rossman, 2013a, 2013b).

The majority of previous peridotite water concentration analyses have been in NAMs from continental xenoliths and a few oceanic xenoliths (see Peslier, 2010, for a review).

Water concentrations in abyssal peridotites have only been measured in three previous studies (Gose et al., 2009; Peslier, 2010; Schmädicke et al., 2011) and no data for orogenic or ophiolitic peridotites are reported in the literature. Abyssal peridotites refer to samples collected on the seafloor either at mid-ocean ridges or in subduction zones. They are depleted residues of the melting that forms oceanic crust and typically have lower trace element concentrations than peridotite xenoliths from continental lithosphere. Ophiolitic and orogenic peridotites refer to obducted pieces of oceanic lithosphere - with or without the overlying crust - and typically are from supra-subduction zone settings.

The lack of water measurements in abyssal, orogenic and ophiolitic peridotites is due

to (i) concerns about the effects of alteration, mainly due to the formation of serpentine and (ii) concerns about diffusive loss of water during ascent to the surface. In xenoliths, olivine typically looses water during ascent to the surface, as H⁺ diffuses rapidly in this mineral (e.g., Kohlstedt & Mackwell, 1998). The general exceptions are kimberlite xenoliths, which are brought rapidly to the surface from very deep and sometimes preserve their original water concentrations (Demouchy et al., 2006; Peslier et al., 2008, 2012). In contrast, abyssal and orogenic peridotites are emplaced at plate spreading rates (i.e., emplacement timescales are much slower compared to xenoliths), but tectonically exposed peridotite massifs are also ~6 orders of magnitude larger in size than xenoliths.

In this paper, we use SIMS to measure water concentrations in olivine, orthopyroxene, and clinopyroxene from a variety of peridotites, with a focus on the oceanic mantle. Samples include abyssal peridotites from the Gakkel Ridge, Southwest Indian Ridge, and Tonga Trench, xenoliths from Pali Aike, Spitsbergen, and Samoa, and orogenic peridotites from the Josephine Peridotite. We demonstrate that olivine in all samples has lost water, but that orthopyroxene and clinopyroxene maintain their high temperature water concentrations. Except at very high degrees of alteration, hydrothermal processes do not affect mineral water concentrations.

2. Geologic Setting of Samples

Peridotites investigated encompass xenoliths, orogenic peridotites and abyssal peridotites (Table 1). All xenoliths are fresh, while orogenic samples from the Josephine Peridotite have low degrees of serpentinization and abyssal peridotites range from fresh to highly altered. Continental xenoliths are from Pali Aike, Patagonia (Stern et al., 1989, 1999) and Sverrefjell, Spitsbergen (Amundsen et al., 1987b; Ionov et al., 1993, 1996), while

oceanic xenoliths are from Savai'i, Samoa (Hauri et al., 1993; Hauri and Hart, 1994).

Carbonatite metasomatism has been documented in xenoliths from Spitsbergen and Samoa, including a Samoa sample in this study (SAV-1-28). Orogenic samples are from shear zones in the Josephine Peridotite, Oregon (Kelemen and Dick, 1995; Warren et al., 2008), for which water content variations are expected based on changes in olivine lattice preferred orientations (Skemer et al., 2010).

Abyssal peridotites are from the Gakkel Ridge (Michael et al., 2003), the Southwest Indian Ridge (SWIR; Standish et al., 2008; Warren et al., 2009), and the Tonga Trench (Fisher & Engel, 1969; Wright et al., 2000). Gakkel and Tonga samples are unaltered (Fig. 1) and were specifically included to provide a comparison to altered abyssal peridotites. In contrast, SWIR samples have moderate to high degrees of alteration (Fig. 1), but are well described in terms of major and trace elements, as well as Nd and Sr isotopic compositions (Warren et al., 2009).

3. Methods

A total of 21 olivines, 62 orthopyroxenes and 10 clinopyroxenes were hand picked from 31 peridotites. Grains were mounted in size order from largest to smallest by pressing into indium contained in 1" diameter aluminum disks (Koga et al., 2003; Aubaud et al., 2007). Grinding on SiC grits exposed the approximate center of each grain. On each of the three mounts prepared, a piece of synthetic forsterite was included for use in monitoring background water concentrations (Koga et al., 2003). Once all grains were mounted, the samples were polished using diamond suspensions down to 1 μm. The mounts were cleaned in ethanol and placed in a vacuum oven at 50 °C for at least 12 hours. Samples were removed from the vacuum oven and coated with gold immediately prior to analytical sessions.

Samples were analyzed using the Cameca 6f SIMS at the Department of Terrestrial Magnetism, Carnegie Institution of Washington (Hauri et al., 2002; Koga et al., 2003). Analysis of water in NAMs requires minimal amounts of background volatiles, as monitored by the vacuum pressure in the sample chamber, which should be <10⁻⁹ Torr. To achieve this, the SIMS underwent a 24 hr bake-out prior to each analytical session. The machine was calibrated using a primary set of glass standards, followed by a secondary set of NAMspecific standards to create working curves for olivine, orthopyroxene and clinopyroxene. To further maintain the ultra-high vacuum, sample mounts were introduced into the exchange chamber at least 12 hr prior to insertion into the main sample chamber. Sample mounts were left in the main sample chamber for an additional 12 hr prior to data collection. In general, increases in background H₂O concentrations correlate with increases in sample chamber pressure.

Analyses were made using a rastered Cs⁺ beam with a current of 15-20 nA. The sputter crater was 30-40 µm, but the smallest field aperture was used to limit ion collection to the central 10 µm diameter area. Using the electron multiplier, the masses ¹²C, ¹⁶O¹H, ¹⁹F, ³⁰Si, ³¹P, ³²S and ³⁵Cl were cycled through to collect 5 blocks of data. Intensities of ¹²C/³⁰Si, ³²S/³⁰Si and ³⁵Cl/³⁰Si were used to monitor for contamination. While grains were checked for optical purity using a petrographic microscope prior to analysis, values of these ratios above background were taken as an indicator of inclusions, fractures, or foreign material and were excluded from the dataset. In addition, only analyses with steady count rates, as indicated by low standard deviations in ¹⁶O¹H /³⁰Si, ¹⁹F/³⁰Si and ³¹P/³⁰Si, were included in the dataset (Table 2). Analysis of P was only included in the third analytical session.

Water concentrations were calculated by establishing working curves for olivine,

Opx, and Cpx using standards calibrated by Koga et al. (2003) and Aubaud et al. (2007). Standards used for olivine were: KLV-23, GRR1012, ROM177, ROM250-2, ROM250-13; for Opx: A288, Enstatite-India, KBH-1, ROM273-OG2; for Cpx: CM68, PMR-53, ROM273-10, ROM273-16, ROM273-21. F and P concentrations were determined using basalt glass working curves (Hauri et al., 2002), as no NAM-specific standards are available for these elements. Standards used were: 519-4-1, 1654-3, 1833-1, 1833-11, 1846-12, D30-1, WOK28-3.

The water concentration of the olivine standards is uncertain due to recent revisions in the FTIR calibration upon which some of the standards are based (Kovács et al., 2010; Withers et al., 2012) and due to heterogeneity in at least one of the olivine standards (KLV-23). However, previous studies have demonstrated that SIMS working curves for olivine and Opx are identical within analytical uncertainty, suggesting similar matrix effects (Koga et al., 2003; Kovács et al., 2010; Withers et al., 2011; Mosenfelder & Rossman, 2013a). We also observed similar working curves for Opx and olivine, and therefore used the Opx working curve to determine olivine water concentrations. Ultimately, uncertainties with respect to the olivine calibration are unimportant – in this study – as olivine does not preserve mantle water concentrations (discussed below).

Analyses were corrected for background concentrations of H_2O , F and P by subtracting the concentrations measured in a synthetic forsterite crystal, SynFo68, which contains 40 ppb H_2O (determined by FTIR; Koga et al., 2003). The measured water concentration in SynFo68 provides an indication of the background water level in the mass spectrometer, which varied by session and sample mount. Each block of 10 sample analyses was bracketed by an analysis of SynFo68. Background water was 7.2 ± 0.7 ppm (n=7) for the

first sample mount; from 8.4 ± 0.3 ppm (n=15) to 14 ± 2 ppm (n=2) for the second mount; from 15 ± 3 ppm (n=15) to 20 ± 2 ppm (n=5) for the third mount. Background corrections for F and P were applied assuming that SynFo68 contains none of these elements. Across three analytical sessions, background concentrations of F were: 0.23 ± 0.02 ppm (n=7), 0.21 ± 0.01 ppm (n=15), and 0.085 ± 0.007 ppm (n=15). The background concentration for P, which was only collected in the third session, was 1.01 ± 0.03 ppm (n=15). All data reported in Table 2 and supplementary Tables S1-S3 have been background corrected.

Analytical error for individual volatile analyses (Tables S1-S3) was determined in various ways, including: (i) variations in background water concentrations, (ii) analytical reproducibility, and (iii) count statistics. The error in background water concentration is given by the standard deviation in SynFo68 concentrations for a given group of analyses.

Reproducibility for water concentrations was determined from 8 repeat analyses of a homogeneous olivine grain from sample BMRG08-98-2-1, which gave a value of 3.8 ± 0.3 ppm (25), equivalent to 9% reproducibility. For H₂O, the precision indicated by the count statistics was generally better than the analytical reproducibility. An estimate of analytical reproducibility for F and P is provided by repeat analyses of grains from Pali Aike xenolith TMO. For olivine, 5 repeat analyses of a grain gave 1% reproducibility for F and 3% reproducibility for P. For Opx, 3 repeat analyses gave 1% reproducibility for F, but 10% reproducibility for P. For Cpx, 9 repeat analyses gave 7% reproducibility for both F and P. For comparison, the standard deviation of background concentrations as measured in SynFo68 is 7%-15% for F and 3% for P. Due to the low concentrations of F and P in peridotite minerals, the count statistic error is sometimes greater than the reproducibility.

For individual analyses (Tables S1-S3), the reported analytical error is the error

propagated by combining background error and analytical reproducibility. For the averages of all analyses per sample (Table 2), the reported error is the standard deviation of the average, which is always greater than the analytical error associated with individual analyses. If only one good analysis is available for a sample, the analytical error is used.

Trace element data were collected for a subset of clinopyroxenes in this study using the Cameca 6f SIMS. An O beam with 8-12 nA current and ~75 μm diameter was used with an accelerating voltage of 10 kV and an energy filter offset of -135 V. Working curves were determined using Cpx standards from Eggins et al. (1998) and Norman (1998). The calibration was checked against KH1 Cpx (Irving and Frey, 1984), for which the measured values of trace elements were found to be within 25% of the accepted values (typical for low concentration trace elements). Concentrations of Gd, Dy, Er, Yb and Hf were corrected for oxide interferences, as discussed by Hellebrand et al. (2002).

Major element data were not collected in this study, as they are already available for the SWIR (Warren et al., 2009), Gakkel Ridge (H.J.B. Dick, personal communication, 2007), Josephine Peridotite (Skemer et al., 2010), Samoa xenoliths (Hauri & Hart, 1994) and Pali Aike xenoliths (Stern et al., 1989).

4. Results

Results from the analysis of H₂O, F and P in olivine, Opx and Cpx from 31 peridotites are given in Table 2. Results are averaged by sample, with data for individual analyses given in Tables S1-S3. Water concentrations in olivine vary from 0.4-22 ppm, in Opx from 2-521 ppm and in Cpx from 42-735 ppm (Fig. 2). Concentrations of F range from 0.02-2 ppm in olivine, 0.1-26 ppm in Opx and 0.1-66 ppm in Cpx (Fig. 3). Several samples

were below detection limit for F (Table 1), which is estimated as 0.01 ppm for olivine and 0.1 ppm for pyroxenes. The concentration of P in olivine was only measured in the Pali Aike samples, which have an average concentration of 48 ppm. For pyroxenes, P – which was only measured in Pali Aike and SWIR pyroxenite-veined peridotites – ranged from 1-15 ppm in Opx and 5-32 ppm in Cpx (Fig. 3).

Water concentrations measured in this study are within the range of previous measurements of olivine and pyroxenes from peridotite xenoliths (e.g., Peslier et al., 2002; Peslier & Luhr, 2006), as shown in Fig. 2. Data also plot within the range for model upper mantle mineral concentrations (Table 3), calculated from the estimated range of water in the bulk upper mantle (Hirschmann, 2006). However, as discussed below, olivine concentrations are relatively low and appear to have diffusively lost water, whereas pyroxenes provide a robust means of constraining upper mantle water variations.

Two Pali Aike xenoliths were analyzed in order to provide a comparison to previous FTIR data from this locality. Demouchy et al. (2006) measured 28 ± 10 and 32 ± 10 ppm H_2O in two olivine grains from xenolith LS33. For comparison, the two LS33 olivines in this study have 12 ± 3 and 15 ± 6 ppm H_2O (Tables S1-S3). These results are in reasonable agreement given that Demouchy et al. (2006) determined that Pali Aike olivines have undergone variable degrees of diffusive water loss during ascent. Pyroxene data are unfortunately not available for the exact same xenoliths. In Pali Aike xenolith Palix-1, which was measured by FTIR by Demouchy et al. (2006), $Opx=310 \pm 105$ ppm and $Cpx=416 \pm 150$ ppm. For comparison, SIMS analyses in this study give $Opx=216 \pm 18$ ppm, $Cpx=458 \pm 63$ ppm for LS33 and $Opx=287 \pm 9$ ppm, $Cpx=667 \pm 70$ ppm for TMO. These values are in reasonable agreement if some of the variability is assumed to reflect local variations in water

content.

Peridotites from different tectonic environments show distinct ranges in water concentrations (Fig. 2), although the sample set is small. Ridge peridotites extend to very low concentrations, especially when previously published data are included for the Gakkel Sparsely Magmatic Zone (Peslier, 2010) and the Fifteen-Twenty region on the MAR (Schmädicke et al., 2011). Veined peridotites from the SWIR Oblique Segment extend to very low concentrations and have the largest range in water concentrations for any individual location. Subduction zone samples (Tonga Trench and Josephine Peridotite) bracket almost the full range of concentrations, with the Josephine Peridotite having relatively high concentrations whereas Tonga is relatively depleted. Combined with published data, xenoliths have the largest range of concentrations, but they represent many tectonic environments. Oceanic xenoliths from Samoa (this study) and Cape Verde (Bonadiman et al., 2009) overlap the range of seafloor peridotites and have lower concentrations than continental xenoliths.

Pyroxene trace element data are provided in Table 4 and rare earth element (REE) plots are shown in Fig. 4. The SWIR and Gakkel peridotites have typical, depleted patterns for abyssal peridotites, except for the SWIR pyroxenite-veined samples. Josephine and Tonga peridotites are extremely depleted, with some elements below the detection limit (~1 ppb). The xenoliths are variably enriched, reflecting the varied origin of these peridotites.

5. Discussion of Water in Peridotite NAMs

5.1. Effect of alteration on NAMs

A major concern for the analysis of abyssal and orogenic peridotites is the potential

effect of incipient serpentinization, followed by diffusive exchange between serpentine and NAMs. An additional concern is incipient hydration of NAMs at spatial scales not readily identifiable by optical microscopy. We assess the effect of alteration on measured water concentrations by: (i) petrographic analysis; (ii) examining the dataset for analyses that show high C, Cl, or S counts; (iii) diffusion modeling; and (iv) comparison of results between fresh and altered samples.

Samples in this study are a mixture of fresh (Tonga, Gakkel, xenoliths) and altered (SWIR, Josephine) peridotites. In general, xenoliths are the least altered and the SWIR abyssal peridotites are the most altered. Alteration mainly occurs as slight to moderate replacement of olivine by serpentine, brucite, and magnetite. In three SWIR samples (Van7-85-30, Van7-86-27 and Van7-96-16), pyroxenes are partly replaced by tremolite (Fig. 1), which occurs at temperatures >350°C (Bach et al., 2004; Bach & Klein, 2009).

Very strict data filtering was applied to aid in the identification of alteration effects on NAM water concentrations. Of 424 data points collected, 120 analyses (28%) were discarded due to high C, Cl or S counts, or due to large standard deviations in OH, F or P counts. Concentrations for rejected analyses range up to 470 ppm in olivine, 3000 ppm in Opx and 16000 ppm in Cpx. Analyses in which concentrations are only slightly elevated, but analytical indicators are high, probably reflect incipient alteration. Approximately 90% of rejected analyses are from SWIR and Josephine samples, which have the highest levels of alteration (Fig. 1).

Analyses classified as mantle (i.e., pre-alteration) values are strongly dependent on mineral phase. 45% of Cpx analyses are excluded from the final dataset, whereas only 20%

of olivine and 16% of Opx analyses are excluded. Among SWIR samples, comparatively more Cpx was measured in an effort to obtain reliable H₂O concentration data, but only 59 of 129 analyses correspond to mantle water contents. In contrast, Opx produced consistently better data, with 73 of 96 SWIR analyses included in the final dataset. Difficulties with Cpx analyses may reflect a higher rate of incipient alteration, possibly due to wider exsolution lamellae in Cpx in comparison to Opx. Thus, Opx in natural peridotites is the most important NAM for constraining upper mantle water concentrations.

Three of the abyssal peridotites are too altered to produce reliable data: Van7-85-30, Van7-86-27 and Van7-96-16. In these samples, few reliable data were obtained despite many analyses, and even these have relatively high water concentrations: 650-800 ppm H₂O in Cpx and 300-400 ppm in Opx (Fig. 2). Petrographic observation indicates high degrees of alteration, including partial replacement of pyroxene by amphibole. For example, the photomicrograph of Van7-85-30 (Fig. 1E) shows alteration haloes around Opx. Van7-96-16 consists of coarse grained, relatively unaltered regions that are cross cut by fine-grained zones where pyroxenes have been replaced by amphibole and serpentine (Fig. 1F).

Previous Sr isotopic analyses for two of the three highly altered peridotites confirm that they have undergone extensive exchange with seawater. For example, Cpx from Van7-85-30 and Van7-86-27 have $^{87}\text{Sr}/^{86}\text{Sr} > 0.704$ (Warren et al., 2009). In comparison, the upper mantle has $^{87}\text{Sr}/^{86}\text{Sr} \approx 0.702$ and seawater has $^{87}\text{Sr}/^{86}\text{Sr} = 0.709$. All samples from Warren et al. (2009) were extensively leached to remove surficial alteration prior to Sr isotopic analysis. Only Van7-85-30 and Van7-86-27 produced high $^{87}\text{Sr}/^{86}\text{Sr}$, whereas other samples from dredge Van7-85 have $^{87}\text{Sr}/^{86}\text{Sr} \approx 0.702$. Warren et al. (2009) interpreted the elevated $^{87}\text{Sr}/^{86}\text{Sr}$ ratios in Van7-85-30 and Van7-86-27 to reflect extensive reaction with seawater, resulting in

partial replacement of pyroxene by tremolite. Based on these observations, the three highly altered peridotites are excluded from further discussion and analysis.

The high water concentration of pyroxenes in highly altered peridotites indicates that water can be added to NAMs at high levels of alteration. Alteration could also remove water from NAMs, as found in a study by Andrut et al. (2003) of metamorphic diopside, in which dissolved water decreased in the vicinity of amphibole lamellae. However, we did not find any evidence that alteration decreases water concentrations, based on the absence of pyroxene zonation and high water contents in the most altered samples.

Even when alteration is not extensive (i.e., low water/rock ratios), diffusive exchange between serpentine and NAMs could potentially influence olivine and pyroxene water concentrations. Serpentinization typically occurs over the range 50-250°C (Alt et al., 2007) and is generally insignificant above ~330°C (Klein et al., 2009). At 300°C, the hydrogen diffusion coefficient in olivine is ~10⁻²⁶ m²/s (Kohlstedt & Mackwell, 1998; Demouchy et al., 2006), which corresponds to a diffusion distance of only a few microns over tens of millions of years. Similarly, Gose et al. (2011) concluded that, below 300°C, hydrogen diffusion is too slow in Opx for serpentinization to change water concentrations in mm-sized crystals. In addition, they used IR mapping to show that defect water is relatively homogeneously distributed in Opx from MAR peridotites and is unrelated to the presence of serpentine in grain cracks. Thus, incipient serpentinization is not expected to increase water concentrations throughout peridotite minerals.

Comparison of altered peridotites to unaltered peridotites also suggests that low levels of alteration do not influence NAM water concentrations. For example, the two Gakkel

peridotites – which are very fresh (Fig. 1) – have Opx H_2O concentrations of ~100-150 ppm. Among the altered SWIR peridotites (excluding the three highly altered samples), unveined peridotites have ~150-200 ppm, while the peridotite matrix and pyroxenite veins in a set of veined peridotites have ~20-150 ppm. If the difference in water concentration is due to variable degrees of alteration – instead of variations related to tectonic setting – then the SWIR peridotites should have uniformly higher water concentrations, which they do not. Thus, we conclude that abyssal and orogenic peridotites can be analyzed for volatile concentrations, as long as they have low to moderate levels of alteration and analyses are not made in the vicinity of incipient serpentinization.

5.2. Diffusive loss of water during peridotite emplacement

A second major concern when analyzing peridotite NAMs is that the minerals have diffusively lost water during emplacement. Xenolith studies have often found that water in olivine is diffusively lost during emplacement (e.g., Demouchy et al., 2006; Peslier & Luhr, 2006; Li et al., 2008; Denis et al., 2013). In this study, olivines also appear to have lost water, while pyroxenes have maintained their pre-emplacement compositions. This conclusion is based on three lines of evidence: (i) water concentrations are >100 ppm in most pyroxenes, but are <15 ppm in olivines (Fig. 2); (ii) zonation occurs in some olivines, but not in any pyroxene (Fig. 5); and (iii) partitioning between Cpx and Opx suggests equilibrium, whereas partitioning between olivine and Cpx or Opx indicates disequilibrium (Fig. 6).

Water zonation in olivine is shown in Fig. 5 for grains with both core and rim analyses. Olivine plots significantly off the 1:1 correlation line, as many cores have higher concentrations than rims – most notably when cores have >10 ppm $\rm H_2O$. Disequilibrium occurs between olivine cores and rims in all peridotite types (xenolith, orogenic and abyssal).

In addition, olivine water concentrations are <15 ppm for all samples. These two observations are interpreted as evidence for diffusive loss of water from olivine during peridotite emplacement.

Pyroxenes do not appear to have undergone diffusive water loss. In Fig. 5, pyroxene cores and rims scatter around the 1:1 correlation line. In particular, Opx shows the best correspondence between cores and rims, with only 2 points plotting significantly off the line. Both of these points are from sample Van7-96-18M, which is the matrix of a pyroxenite-veined peridotite. The variability in this sample may reflect magmatic reaction between the host peridotite and lower concentration melts that produced pyroxene with low water contents.

Mineral-mineral partition coefficients ($D_{H2O}^{Min/Min}$) also support the interpretation that olivine has lost water, but that pyroxenes have not. In Fig. 6, $D_{H2O}^{Cpx/Opx}$ shows little variation and is similar in value to experimentally determined partition coefficients, suggesting that pyroxenes are in equilibrium. In contrast, $D_{H2O}^{Ol/Opx}$ and $D_{H2O}^{Ol/Cpx}$ cover a large range of values in natural samples, with many plotting at lower olivine water contents than predicted by experimental $D_{H2O}^{Ol/Opx}$ and $D_{H2O}^{Ol/Cpx}$. Similar observations have been made in other xenolith studies (e.g., Xia et al., 2010; Yu et al., 2011).

The low water concentration in a subset of the SWIR veined samples (Fig. 2), which is most pronounced in pyroxenite sample Van7-96-09, could be interpreted as diffusive water loss. However, other samples in this dredge have concentrations up to 160 ppm in Opx and 650 ppm in Cpx. As all samples from a dredge have the same emplacement history, it is unlikely that they had different degassing histories. Additionally, the pyroxene grain size in

Van7-96-09 is larger than any of the other samples (Fig. 1D), meaning it is the least likely to record diffusive water loss. Hence, the low H₂O concentrations in Van7-96-09 are interpreted as having a high-temperature origin, with variations among samples in this dredge best explained by melt-peridotite interaction.

5.3. Comparison to experimental diffusion data

As discussed above, natural pyroxenes in this study appear to have retained their mantle water contents, whereas olivines have lost water. Other xenolith studies have made similar observations (e.g., Peslier et al., 2002, 2012; Grant et al., 2007a; Peslier, 2010; Xia et al., 2010; Sundvall & Stalder, 2011; Yu et al., 2011). Profiles across magmatic Cpx phenocrysts also indicate minimal water loss (Wade et al., 2008; Nazzareni et al., 2011; Sundvall & Stalder, 2011). However, these observations are in disagreement with diffusion experiments for hydrogen, which have found D_H≈10⁻⁹-10⁻¹² m²/s at 1000°C for both olivine and pyroxene (Mackwell & Kohlstedt, 1990; Ingrin et al., 1995; Kohlstedt & Mackwell, 1998: Hercule & Ingrin, 1999; Woods et al., 2000; Stalder & Skogby, 2003; Demouchy & Mackwell, 2006; Ingrin & Blanchard, 2006; Farver, 2010). The symbol D_H is used here to refer to hydrogen diffusion coefficients, while $D_{H2O}^{Ol/Opx}$, $D_{H2O}^{Ol/Cpx}$, and $D_{H2O}^{Cpx/Opx}$ refer to water partition coefficients. If hydrogen diffuses out of pyroxene at the same rate as olivine, then pyroxenes should not have such high water concentrations. For example, for $D_H=10^{-12}~\text{m}^2/\text{s}$ at 1000°C, pyroxene grains of 1 cm radius would re-equilibrate in <3 years. In order for pyroxenes to retain water for >1 My, the effective diffusion coefficient at 1000°C needs to be <10⁻¹⁸ m²/s, or at least 6 orders of magnitude lower.

Possible explanations for the discrepancy between experimentally-determined diffusion rates and observations of natural pyroxenes fall into two categories: (i) differences

between experimental conditions and mantle conditions (e.g., Sundvall & Stalder, 2011) and (ii) hydrogen loss that is rate-limited by other mechanisms (e.g., Grant et al., 2007a; Sundvall & Skogby, 2011; Peslier et al., 2012). In contrast to olivine, experimental diffusion data for pyroxene has only been collected at room pressure and often at reducing conditions relative to the upper mantle (Ingrin et al., 1995; Hercule & Ingrin, 1999; Woods et al., 2000; Stalder & Skogby, 2003; Ingrin & Blanchard, 2006). The extent to which these diffusion coefficients are applicable at mantle conditions is thus unconstrained. However, making measurements at the correct conditions may not necessarily result in diffusion coefficients that are six (or more) orders of magnitude slower.

The second explanation for the discrepancy between diffusion experiments and natural pyroxenes is that H dehydration is rate-limited by the movement of either electron holes or cations. Hercule & Ingrin (1999) suggested that the slower diffusion of H in pyroxene during incorporation/extraction experiments, in comparison to self-diffusion experiments, reflects H mobility controlled by electron hole counterflux. In this mechanism, the movement of electron holes depends on pyroxene Fe content, with increasing Fe content yielding increased electron hole mobility due to the exchange reaction: $Fe^{3+} + O^{2-} + 1/2H_2 \leftrightarrow Fe^{2+} + OH^-$. Experiments suggest that H diffusion decreases by approximately two orders of magnitude at low Fe contents, but that this difference disappears with increasing Fe (Hercule & Ingrin, 1999; Woods et al., 2000; Sundvall et al., 2009).

In addition to Fe content, the movement of cations such as Al or Cr may also be rate limiting for dehydration. For example, significant amounts of hydrogen incorporation in pyroxene can occur by the coupled exchanges of (i) ^{IV}Al³⁺ and H⁺ for Si⁴⁺ (Skogby et al., 1990; Rauch & Keppler, 2002; Stalder & Skogby, 2002; Kohn et al., 2005; Hauri et al., 2006;

Skogby, 2006; Karato, 2008) and (ii) $^{VI}Al^{3+}$ and H^+ for $2Mg^{2+}$ (Carpenter, 2003; Stalder & Skogby, 2002; Stalder, 2004; Kohn et al., 2005). Cpx in this study contains 2-8 wt% Al_2O_3 and Opx contains 2-6 wt% Al_2O_3 , so Al-coupled mechanisms for hydrogen incorporation/extraction should be important.

In the absence of pyroxene diffusion data over a large range of pressures, fugacities and compositions, we suggest that retention of H in pyroxenes may be largely due to cation-limited diffusion. Many studies of H diffusion in NAMs have identified both fast and slow diffusion processes, with fast diffusion typically occurring by the exchange of protons with electron holes (e.g., Kohlstedt & Mackwell, 1998, 1999). Hence, the possibility remains that some fraction of water is lost very quickly from pyroxenes (and olivines), but that the majority is left behind in the case of pyroxenes. Our samples represent a wide range of tectonic environments (ocean ridges, subduction zones), surface exposures (subaerial to submarine), and exhumation rates (orogenic uplift, volcanic eruption), yet all have the same features of homogeneous pyroxenes and variably dehydrated olivines. Unless exhumation rates and accompanying evolutions in water fugacity coincidentally produced this set of data, we find it unlikely that such variety would not produce obvious differences with respect to tectonic setting, surface exposure, or mode of peridotite delivery to the surface.

5.4. Olivine-Pyroxene Partition Coefficients

The amount of water in olivine at mantle conditions is necessary for calculating mantle properties such as bulk mantle water content and viscosity. The original amount of water in olivine can be determined from either the Opx or Cpx water concentration if the mineral-mineral partition coefficient is known.

Estimates for partition coefficients between olivine, Opx and Cpx are shown in Fig 6. For samples in this study, $D_{H2O}^{Ol/Opx}$ has a range of 0.01-0.06, with an average value of 0.04±0.01 (N=12 samples), while $D_{H2O}^{Ol/Cpx}$ has a range of 0.01-0.03, with an average of 0.02±0.01 (N=6). These values are relatively low, which is assumed to be due to water loss from olivine. For comparison, the xenolith average is $D_{H2O}^{Ol/Opx}$ =0.11±0.10 (N=71) and $D_{H2O}^{Ol/Cpx}$ =0.05±0.06 (N=65), based on a literature compilation (Bell & Rossman, 1992; Peslier et al., 2002; Demouchy et al., 2006; Peslier & Luhr, 2006; Aubaud et al., 2007; Grant et al., 2007b; Falus et al., 2008; Li et al., 2008; Yang et al., 2008; Bonadiman et al., 2009; Xia et al., 2010). The large standard deviation for the average xenolith partition coefficients may be partly due to variations in FTIR data reduction methodologies and the inclusion of partially degassed olivines in the dataset. Hirth & Kohlstedt (1996) estimated $D_{H2O}^{Ol/Opx}$ =0.2 and $D_{H2O}^{Ol/Cpx}$ =0.1, based on a combination of available data from natural and experimental samples.

Experimental data provide a better estimate of olivine-pyroxene partition coefficients, as experiments are cooled fast enough that loss of water from olivine – at least by the metal vacancy exchange mechanism – does not occur. Water partition coefficients vary as a function of pressure and Al content (e.g., Hauri et al., 2006; Ardia et al., 2012). Current estimates from low-pressure (<2 GPa) alumina-bearing experiments analyzed by SIMS are $D_{H20}^{Ol/Opx} = 0.11 \pm 0.03$ (N=12) and $D_{H20}^{Ol/Opx} = 0.07 \pm 0.02$ (N=9) (Fig.6, using data from Aubaud et al., 2004; Hauri et al., 2006; Tenner et al., 2009). Additional $D_{H20}^{Ol/Opx}$ experimental data are available in Grant et al. (2006, 2007a), with $D_{H20}^{Ol/Opx} = 0.34 \pm 0.21$ based on nine experiments, of which seven are nominally alumina-free. The Grant datasets were collected by FTIR and plot significantly off the trend of the other experimental datasets. This difference may reflect uncertainties in the baseline correction, as discussed by Grant et al. (2006), and in the

absorption coefficients used to convert FTIR spectra into absolute water concentrations, which have undergone revisions in recent years (Withers et al., 2012; Mosenfelder & Rossman, 2013a). Hence, the Grant data are excluded from the average values for olivine-pyroxene partitioning. In addition, partition coefficients should vary as a function of temperature, oxidation state, and water fugacity (Dai & Karato, 2009), but data are not available to constrain these effects. Using the low-pressure alumina-bearing experiments, the best available experimental estimate for $D_{H2O}^{Ol/Opx}$ is 0.11. We use this value below to calculate high temperature olivine water concentrations based on Opx water concentrations.

5.5. Cpx-Opx Partition Coefficients

The partition coefficient between Cpx and Opx has an average value in this study of $D_{H2O}^{Cpx/Opx}$ =2.4 ±0.3 (N=11), excluding SWIR veined peridotites. In Fig. 6, our dataset is compared to published datasets for pyroxenes in experiments and xenoliths. Alumina-bearing experimental data give $D_{H2O}^{Cpx/Opx}$ =1.3 ±0.3 (N=10) (Aubaud et al., 2004; Hauri et al., 2006; Tenner et al 2009). The larger number of published xenolith analyses give $D_{H2O}^{Cpx/Opx}$ =2.6 ±0.9 (N=141), in agreement with results of this study. The combined value for natural samples (literature data plus our data) is $D_{H2O}^{Cpx/Opx}$ =2.6 ± 0.9 (N=152).

The two separate $D_{H2O}^{Cpx/Opx}$ trends (Fig. 6) when comparing experiments to natural samples suggest a systematic difference. The lower experimental value for Cpx/Opx partitioning could result from differences in major element compositions relative to natural pyroxenes. For example, the charge-coupled substitution of aluminum onto the silica tetrahedral site (Si⁴⁺ = IV Al³⁺ + H⁺) is one of the mechanisms for the incorporation of water into pyroxenes (e.g., Rauch & Keppler, 2002; Kohn et al., 2005). However, in Fig. 7, $D_{H2O}^{Cpx/Opx}$

does not correlate with $^{IV}Al^{3+}$ in Opx or Cpx for natural samples. Experimentally determined values for $D_{H2O}^{Cpx/Opx}$ show only a weak correlation with Opx $^{IV}Al^{3+}$ and no correlation with Cpx $^{IV}Al^{3+}$. However, the proportion of $^{IV}Al^{3+}$ on tetrahedral sites in Opx versus Cpx is similar in both experiments and natural samples (Fig. 7C). In contrast, experiments contain less Cr^{3+} on the M1 site in Cpx compared to Opx (Fig. 7D). Experimental Cpx also has more Fe^{2+} on the M2 site when compared to Opx (Fig. 7E), but systematic differences are not observed for Fe^{2+} on the M1 site and for Fe^{3+} on either site. Other cations, such as Ti^{4+} , do not show any systematic offset between experiments and natural samples. The difference in Cr^{3+} and Fe^{2+} may explain the slightly higher value for $D_{H2O}^{Cpx/Opx}$ in natural samples in comparison to experiments. However, caution is necessary in using Fe speciation and site occupancy that is only constrained by electron microprobe data. Dyar et al. (1989) have shown that Mössbauer analysis is necessary to fully constrain this in pyroxenes.

Other possible causes of the difference between experimental and natural $D_{H2O}^{Cpx/Opx}$ are (i) differences in total water content; (ii) differences in temperature and cooling rate between the two systems; and (iii) differences in oxygen fugacity. Although most experiments were H_2O -undersaturated, the H_2O fugacity is probably higher than that for natural samples, as indicated in Fig. 6 by higher water concentrations in experimental pyroxenes. If there is more than one H substitution mechanism (e.g., coupled $^{IV}Al^{3+}$ substitution and coupled metal vacancy substitution), these could have different dependencies on total water fugacity. While experimental data does not show evidence for this (Hauri et al., 2006), such a dependency is required in thermodynamic models for water solubility in pyroxenes under water-saturated conditions (Keppler & Bolfan-Casanova, 2006). Higher Fe^{3+} in experimental pyroxenes relative to natural pyroxenes could also drive differences in $D_{H2O}^{Cpx/Opx}$. When buffered, experiments are typically conducted around Ni-NiO, whereas the mantle has an oxygen

fugacity near the quartz-fayalite-magnetite buffer (Wood et al., 1990). The influence of Fe³⁺ on partitioning has not been examined experimentally and is thus unconstrained.

Pyroxenites and pyroxenite-veined peridotites from dredge Van7-96 plot off the Cpx/Opx partitioning trend in Fig. 6. Cpx and Opx in two samples appear to be in disequilibrium, with $D_{H2O}^{Cpx/Opx}$ >20. Among the other veined samples, $D_{H2O}^{Cpx/Opx}$ =4.6 ±1.5 (N=6), which is significantly higher than the partition coefficient for unveined samples. The higher $D_{H2O}^{Cpx/Opx}$ in pyroxenitic samples may be due to higher Cpx aluminum contents, incomplete equilibration during formation of the pyroxenite veins, or differences in oxygen fugacity.

5.6. Bulk Mantle Water Concentrations

Bulk mantle water contents can be estimated using the modal abundances of upper mantle minerals, measured water concentrations, and partition coefficients (Fig. 6). For the calculation, olivine water concentrations were estimated assuming $D_{H2O}^{Ol/Opx}$ =0.11, which is the average value from low-pressure alumina-bearing experiments (Aubaud et al., 2004; Hauri et al., 2006; Tenner et al., 2009). For five samples without measured Cpx water concentrations (of which three contain <1% modal Cpx), values were estimated assuming $D_{H2O}^{Cpx/Opx}$ =2.6, which is the average value from xenoliths in the literature (see Fig. 2 for references).

Variations in calculated water concentrations for olivine and bulk rock peridotites are shown in Fig. 8. Calculated olivine concentrations range from 8-34 ppm H₂O for samples in this study (Table 6) and from 1-51 ppm for xenoliths from the literature. Calculated olivine concentrations are within a reasonable range compared to estimates of upper mantle olivine (8-32 ppm; Table 3). However, concentrations in ridge peridotites are higher than predicted for the residues of melting, which is discussed in detail in the next section.

The range of calculated bulk rock concentrations for samples in this study is 18-220 ppm H₂O (Table 6), which compares favorably to the pre-melting upper mantle range of 50-200 ppm H₂O (Hirschmann, 2006). Unveined abyssal peridotites contain 18-118 ppm, while the Pali Aike continental xenolith has 125 ppm and the Samoa oceanic xenoliths have 31-51 ppm. SWIR pyroxenite-veins cover the largest range of water concentrations, from 36 to 220 ppm, due to the abundance of pyroxene in these samples and the large variation in pyroxene water contents (9-162 ppm in Opx).

Calculated bulk water concentrations are plotted as a function of peridotite depletion in Fig. 9. Cpx mode and bulk Al₂O₃ both decrease during melting, while spinel Cr# increases during melting. Our data suggest that bulk water concentrations are correlated with the degree of peridotite depletion. Among unveined abyssal peridotites, bulk water concentrations have correlation coefficients of 0.99 with modal Cpx, 0.94 with bulk Al₂O₃ and -0.97 with spinel Cr#. Xenoliths in this study also plot on these trends, though they are not included in the regressions in Fig. 9. The correlation between bulk water and modal Cpx is not simply due to Cpx modal abundance: although Cpx has an average of 2.6 times more water than Opx, Opx is 2-10 times more abundant than Cpx, and there is no correlation between Opx and Cpx modes.

We also calculated bulk peridotite water concentrations for published xenolith datasets for which modal data is available (143 samples; Fig. 9). In studies by Peslier and coworkers (Peslier et al., 2002; Peslier & Luhr, 2006), bulk water is weakly correlated with Cpx mode, bulk Al_2O_3 and spinel Cr# (r=0.88, 0.73, -0.70, respectively). Other xenolith datasets show no correlation. These samples are mainly continental xenoliths, so the lack of

systematic variations may reflect various episodes of melt and fluid refertilization (e.g., Peslier, 2010). Alternatively, the lack of strong correlations may reflect uncertainties in FTIR data reduction, including the choice of calibration, baseline fitting of spectra, and effects of cracks, alteration and microscopic inclusions (e.g., Bell et al., 2003; Aubaud et al., 2009; Kovács et al., 2010; Stalder et al., 2012; Mosenfelder & Rossman, 2013a, 2013b; Withers, 2013).

5.7. Variation of H₂O and Ce in peridotites

The trace element Ce has been used as a proxy for water concentration in basalts, as the relatively constant H₂O/Ce ratio in MORBs suggests similar partitioning during melting (Michael et al., 1995). Estimates for the amount of water in the upper mantle are based on the H₂O/Ce ratio, which has a range of 150-250 in basalts (Michael, 1995; Saal et al., 2002), combined with estimates of upper mantle Ce (0.4-0.7 ppm; Salters & Stracke, 2004; Workman & Hart, 2005). The MORB source is thus estimated to have 50-200 ppm H₂O, while OIB mantle is estimated to have 100-300 ppm H₂O (Hirschmann, 2006). In Fig. 10, estimates for H₂O and Ce in the MORB mantle source are shown as grey shaded fields.

Peridotites show a considerable range of H₂O/Ce ratios, at both the mineral level (Fig. 10A) and the bulk rock level (Fig. 10B). To explore the implications of H₂O-Ce variations in peridotites, we ran nonmodal fractional and dynamic melting models (Fig. 11). As a first step, the degree of melting represented by abyssal peridotite REE concentrations was modeled using equations from Zou (1998), an initial mantle composition from Workman & Hart (2005), and melting reactions as referenced in Table 7. Bulk rock REE concentrations (Fig. 11A) were calculated from Cpx trace element concentrations using mineral-mineral partition coefficients (Kelemen et al., 2003) and mineral modes. For SWIR samples, REE patterns can

be reproduced by \sim 1-6% melting in the spinel field using either fractional or dynamic melting models. For dynamic melting, a fit was obtained using a residual porosity (ϕ) of 0.1%, with larger porosity values yielding worse fits.

In contrast to SWIR samples, the Tonga Trench peridotites are difficult to fit using either fractional or dynamic melting models. While heavy REEs can be reproduced by ~12.5% melting, light REEs have concentrations that are too high to be fit, even at high values of ϕ (~2%). Tonga peridotites are overall more complicated than ridge peridotites, as indicated by spinel Cr# >60 and bulk rock Al₂O₃ <1 wt%. These chemical characteristics suggest a melting history that possibly involved fluxing by melt and fluids in the subduction zone.

Using estimates for degree of melting from the REE modeling of SWIR samples, the variation in bulk peridotite Ce and H_2O was modeled (Fig. 11B). As the difference between dynamic and fractional melting models is small, only the fractional model was used to explore variations in H_2O during melting. Various sets of H_2O partition coefficients were tested in the model, as published partition coefficients (Table 7) are not internally consistent: i.e., $D_{H2O}^{Cpx/Melt} / D_{H2O}^{Opx/Melt} \neq D_{H2O}^{Cpx/Opx}$, etc. This discrepancy is likely due to the difficulty of running multiply saturated experiments, meaning that H_2O activities are not the same as that imposed by the full peridotite assemblage. To overcome the inconsistency among partition coefficients, we calculated $D_{H2O}^{Min/Melt}$ for Cpx and olivine based on $D_{H2O}^{Opx/Melt} = 0.018$ (O'Leary et al., 2010), $D_{H2O}^{Ol/Opx} = 0.11$, and $D_{H2O}^{Cpx/Opx} = 2.6$. Spinel was assumed to contain no water and was excluded from the calculations. Using different published values for the partition coefficients (Aubaud et al., 2004; Hauri et al., 2006; Kohn & Grant, 2006; Grant et al., 2007a; Hirschmann et al., 2009; Tenner et al., 2009) results in small variations among the

modeled trajectories of the melt residues.

The fractional melting model in Fig. 11B reproduces the H₂O-Ce trend of MORB data along a trajectory of 1-6% melting. The MORB data are slightly offset from the model and a better fit could be achieved by fine-tuning the partition coefficient values and model parameters. However, more significant is the complete mismatch between the trajectory of the melt residue and the peridotite H₂O-Ce dataset. To produce a match would require $D_{H2O}^{Bulk/Melt} > D_{Ce}^{Bulk/Melt}, \text{ whereas MORB and experimental studies have found}$ $D_{H2O}^{Bulk/Melt} < D_{Ce}^{Bulk/Melt} \text{ (Table 7). Furthermore, any set of partition coefficients that reproduces}$ the peridotite data is not able to simultaneously match MORB compositions, regardless of the degree of melting used in the model.

The fractional melting model indicates that the amount of water in abyssal peridotites is higher than expected for residues of melting. However, instantaneous melts in equilibrium with peridotites have reasonable water concentrations. The most depleted peridotite (BMRG08-98-2-1) has 18 ppm $\rm H_2O$ and $D_{\rm H2O}^{\it Bulk/Melt}=0.004$ (calculated from mineral modes and mineral/melt partition coefficients), which corresponds to an equilibrium melt with 0.45 wt% $\rm H_2O$. The most enriched unveined abyssal peridotite (PS86-6-38) has 118 ppm $\rm H_2O$ and $D_{\rm H2O}^{\it Bulk/Melt}=0.012$, which corresponds to an equilibrium melt with 1 wt% $\rm H_2O$. For comparison, MORB glasses have ~0.1-1.5 wt% $\rm H_2O$ (Dixon et al., 2002). The similarity between MORB water concentrations and instantaneous melts in equilibrium with peridotites suggests that peridotite compositions may reflect equilibration with late-stage melts trapped in the shallow mantle. Open-system melting and refertilization has often been invoked to explain concentrations of the light REEs in abyssal and orogenic peridotites (e.g., Godard et al., 1995, 2008; Ozawa & Shimizu, 1995; Vernières et al., 1997; Warren et al., 2009). This

same mechanism may have resulted in the relatively high water content of abyssal peridotites, which would account for the high apparent $D_{H2O}^{Bulk/Melt}$ implied by these peridotites.

If the high water contents of abyssal peridotites are due to late-stage refertilization, this implies that the percolating melt has relatively low Ce (and other REE) concentrations. A high water/low Ce melt does not match many natural magmas, particularly in a ridge setting. However, if a late-stage melt infiltrated peridotite at relatively low temperature, diffusion of H may have been fast enough for re-equilibration while other trace elements diffused too slowly to equilibrate. For example, REEs have pyroxene diffusion coefficients <10⁻²² m²/s at 1000°C (Van Orman et al., 2001; Cherniak & Liang, 2007; Cherniak & Dimanov, 2010), which is orders of magnitude slower than H diffusion at this temperature.

An alternative explanation for the relatively high water contents in abyssal peridotites is that partition coefficients used in the model do not reflect partitioning throughout the melting process (e.g., Kohn & Grant, 2006). In fact, the constant H_2O/Ce ratio in basalts is somewhat surprising given their different mineral hosts in the mantle. In spinel peridotites, the majority of Ce is hosted in Cpx, whereas significant amounts of water are hosted in olivine and Opx in addition to Cpx. This is reflected in the mineral/melt partition coefficients for Ce and H_2O , which demonstrate differences on a mineral-by-mineral basis (Table 7): e.g., $D_{H2O}^{Cpx/Melt} < D_{Ce}^{Cpx/Melt}$, but $D_{H2O}^{Ol/Melt} > D_{Ce}^{Ol/Melt}$ (Kohn & Grant, 2006). Furthermore, water partitioning varies as a function of pressure, water activity, mineral modes and Al_2O_3 content (Hirth & Kohlstedt, 1996; Asimow et al., 2004; Hauri et al., 2006; Tenner et al., 2009, 2012; Ardia et al., 2012). For example, Hauri et al. (2006) estimated that $D_{H2O}^{Bulk/Melt} \approx D_{Ce}^{Bulk/Melt}$ in the spinel peridotite field, but $D_{H2O}^{Bulk/Melt} < D_{Ce}^{Bulk/Melt}$ for melting above 4 GPa in the garnet

lherzolite field. At higher Al_2O_3 contents, pyroxenes have higher values of $D_{H2O}^{Pyx/Melt}$ (e.g., Grant et al., 2007a; O'Leary et al., 2010). Hence, $D_{H2O}^{Bulk/Melt}$ may initially be higher than current estimates due to the high Al_2O_3 content of pyroxenes in fertile mantle. As H_2O and Ce are incompatible elements, peridotites should be sensitive to these effects and potentially record larger ranges of H_2O/Ce ratios than are observed in aggregated MORB melts.

The relationship between water and Ce in our dataset is based on a limited number of samples and may also reflect regional variations in upper mantle composition. Additional peridotite analyses are necessary to fully explore the H₂O-Ce relationship, as well as the systematics observed with other proxies for degree of melting (e.g., Fig. 9).

5.8. Variations in water content by tectonic setting

Depending on tectonic setting, the estimated bulk water concentration of measured samples vary: ridges, Tonga Trench, and oceanic xenoliths have lower concentrations than continental xenoliths and the Josephine Peridotite (Fig. 2 and Fig. 8). Abyssal peridotites have a range of water concentrations, with Gakkel Ridge and MAR peridotites extending to lower water concentrations than SWIR unveined peridotites. The lower water content of Gakkel compared to SWIR is also observed among basalts, as Gakkel basalts have 0.26 ± 0.04 wt% H_2O (Shaw et al., 2010) compared to 0.60 ± 0.20 wt% H_2O in SWIR basalts (Standish et al., 2008). However, any detailed comparison of ridge-scale variations requires analysis of larger sample suites from these regions. Similarly, the variation among continental xenoliths (137-287 ppm H_2O in Opx) in our sample set is smaller than the literature range for xenoliths (8-460 ppm), but this reflects the limited number of locations investigated.

Despite limited sampling, some aspects of the present dataset are significant in the

context of tectonic setting. The first is the contrast in water contents of the two subduction zone sample suites. Specifically, Tonga peridotites have very low water contents (77-116 ppm H₂O in Opx), whereas Josephine peridotites have the highest water contents (168-289 ppm) of samples in this study (Fig. 2). Tonga peridotites were collected at the bottom of the Tonga trench from the Australian Plate, which is over-riding the subducting Pacific Plate (Bloomer & Fisher, 1987; Wright et al., 2000). These peridotites thus represent mantle from the forearc region of a subduction zone, which is typically more compositionally depleted than both mid-ocean ridge and backarc mantle (Arai & Ishimaru, 2008). In contrast, the Josephine Peridotite is suggested to have originated in either a forearc (Dick, 1976; Kelemen et al., 1995) or backarc setting (Harper, 1984). The relatively high water content of the Josephine would favor a backarc, though other trace elements are not similarly enriched (Fig. 4).

The Josephine Peridotite samples have high, but variable, water concentrations, which is important as the principal slip system in olivine changes as a function of water content and shear stress (Jung & Karato, 2001; Jung et al., 2006). At low shear stress, olivine undergoes a transition in slip system around 30 ppm H₂O (500 ppm H/Si), based on olivine deformation experiments (Jung et al., 2006) adjusted for the calibration of Bell et al. (2003). At <30 ppm H₂O, olivine deforms principally by slip on the (010) plane in the [100] direction, which is referred to as Type-A slip or easy slip. At higher water concentrations, the principal slip system in olivine changes to the (001) plane in the [100] direction, which is referred to as Type-E slip. Most of the Josephine samples have calculated olivine water concentrations of <30 ppm, so Type-A slip is expected. However, sample 3925G02 has a high enough water concentration that a transition to Type-E slip is predicted. LPO analyses by Warren et al. (2008) and Skemer et al. (2010) confirm that the low (<30 ppm H₂O) concentration samples

have Type-A olivine fabrics, while sample 3925G02 (with 34 ppm H₂O or 550 ppm H/Si) has a Type-E fabric. These samples are from high-temperature ductile shear zones (Kelemen & Dick, 1995) and increased water contents also correspond to outcrop-scale increases in shear strain. By modeling the effect of water on olivine deformation, Skemer et al. (2013) showed that elevated water contents promoted shear localization in these shear zones.

Variations in olivine water content in the mantle wedge of subduction zones has been proposed as a mechanism behind trench-parallel seismic anisotropy (e.g., Jung & Karato, 2001; Kneller et al., 2005; Ohuchi et al., 2012). Tonga exhibits trench-parallel shear wave splitting in the 19-21°S region of the trench (Smith et al, 2001), which is the location of our samples. One possible explanation is that elevated water in the nose of the mantle wedge has resulted in a change in the olivine slip system, such that the olivine [100] axis is no longer aligned with the flow direction (Jung & Karato, 2001; Kneller et al., 2005). However, this would require water concentrations in olivine that are >30 ppm H₂O (~500 ppm H/Si). As such high water contents are not observed in Tonga peridotites, other mechanisms must be responsible for the observed trench-parallel splitting, such as complex 3-D flow dynamics (e.g., Long & Silver, 2008).

The final notable aspect of the peridotite dataset is the large range in water concentrations among pyroxenite-veined peridotites from SWIR dredge Van7-96. These peridotites and associated pyroxenite veins do not have distinct water concentrations, nor are trace element and isotopic compositions different between vein and host peridotite (Warren et al., 2009). For example, pyroxenite Opx has a concentration range of 9-162 ppm H₂O, while peridotite Opx has a range of 21-147 ppm. (Note that veined peridotites are too small for measurements to be made >10 cm from a vein.) For comparison, dredge Van7-85, located

further east along the ridge, has a more limited range of 145-198 ppm in peridotite Opx. Trace element and radiogenic isotopic compositions of dredge Van7-96 peridotites and pyroxenites have previously been taken as evidence for substantial melt addition to the mantle during passage of the Bouvet hotspot around 15 Ma (Warren et al., 2009; Warren & Shirey, 2012). While plume material is generally estimated to have a water content of 300-1000 ppm, recycled subducted crust in plumes may have only ~60 ppm H₂O (Nadeau et al., 1993; Dixon et al., 2002). Two of the three pyroxenites in this study have extremely low water concentrations of 9-22 ppm in Opx, which corresponds to ~36 H₂O ppm in the bulk pyroxenite. This supports the interpretation that some material in the Bouvet plume is derived from recycled oceanic crust.

5.9. Viscosity Variations

Olivine water concentrations can be used to predict effective viscosity variations in the mantle. Calculated olivine concentrations, based on Opx concentrations, range from 8-34 ppm H₂O (140-550 ppm H/Si) in unveined peridotites and from 1-18 ppm H₂O (16-290 ppm H/Si) in SWIR veined peridotites (Fig. 8). For comparison, xenoliths in the literature range from 1-51 ppm H₂O (16-830 ppm H/Si) in olivine, also calculated from Opx water concentrations.

Olivine in the upper mantle deforms by dislocation creep (e.g., Goetze & Kohlstedt, 1973; Karato et al., 1986; Hirth & Kohlstedt, 1995). Hirth & Kohlstedt (2003) give the olivine dislocation creep flow law as:

$$\dot{\varepsilon} = A\sigma^n C_{OH}^r \exp\left(-\frac{E + PV}{RT}\right)$$

where $\dot{\varepsilon}$ is strain rate, A is a constant, σ is differential stress, n is the stress exponent, C_{OH} is water concentration in ppm H/Si, r is the water concentration exponent, E is activation

energy, V is activation volume and T is absolute temperature. For wet dislocation creep, A=30 (where A has been adjusted for the FTIR calibration of Bell et al., 2003, assuming a correction factor of 2.5), n=3.5, r=1.2, E=480 kJ/mol, and V=11×10⁻⁶ m³/mol (Hirth & Kohlstedt, 2003). When olivine has <3 ppm H₂O (<50 ppm H/Si), the dry flow law is applicable as the concentration of hydrogen is too low for the charge neutrality condition to control the point defect population (Mei & Kohlstedt, 2000). In the dry dislocation creep flow law, the C_{OH}^r term disappears, A=1.1×10⁵, n=3.5, E=530 kJ/mol, and V=18×10⁻⁶ m³/mol (Hirth & Kohlstedt, 2003).

Effective viscosity can be calculated from strain rate using the relationship:

$$\eta = \sigma/\dot{\epsilon}$$

To calculate viscosity from olivine water concentrations, the temperature, pressure and stress of deformation must be known. Spinel peridotites lack good geobarometers, but pressure at shallow depths has a negligible effect on viscosity as activation volume is small. In orogenic and abyssal peridotites, emplacement is slow and temperatures recovered using geothermometers usually record re-equilibration to temperatures a few hundred degrees below the melting temperature. Therefore, instead of using thermobarometry to estimate the pressure-temperature conditions at which each peridotite last equilibrated, effective viscosity was calculated for all samples using a temperature of 1250°C, depth of ~15 km (0.5 GPa), and stress of 0.3 MPa (Table 6). Comparison at these conditions is equivalent to the viscosity within the lithosphere after melting.

Variations in effective viscosity among our samples and literature xenoliths are shown in Fig. 12. For samples with <3 ppm H_2O (<50 ppm H/Si), their viscosity is that of dry dislocation creep, which has a value of 2.5×10^{21} Pa s at $1250^{\circ}C$ and 0.5 GPa. The viscosity of

the most water-rich sample in this study, from the Josephine Peridotite, is 6×10^{19} Pa s, which is over an order of magnitude lower than the dry viscosity. Upper mantle viscosity is $6-30\times10^{19}$ Pa s, based on the Hirschmann (2006) estimate of 50-200 ppm H₂O in bulk upper mantle (i.e., pre-melting mantle). If these calculations are made at 1350° C and 100 km (3.3 GPa), which roughly corresponds to the lithosphere-asthenosphere boundary, then predicted viscosities decrease: nominally dry samples are 2×10^{21} Pa s, while the wettest sample is 1.5×10^{19} Pa s.

6. Discussion of phosphorus in peridotites

This study provides preliminary constraints on the concentration of P in peridotite minerals following melting, based on the analysis of P in Pali Aike xenoliths and SWIR pyroxenite-veined peridotites. The Pali Aike xenoliths have an average P concentration of 48 ppm in olivine, 7 ppm in Opx, and 25 ppm in Cpx. The concentration of P in the pyroxenite-veined peridotites ranges from 1-15 ppm in Opx and 5-29 ppm in Cpx (Fig. 3). Extensive literature data does not exist for P in mantle peridotites. Limited measurements by LA-ICPMS have found that P ranges from 5-79 ppm in olivine, 16-40 ppm in Opx, and 9-148 ppm in Cpx (e.g., Witt-Eickschen & O'Neill, 2005; Mallmann et al., 2009; De Hoog et al., 2010). These studies include xenoliths with a range of compositions, from spinel and garnet lherzolites to amphibole-bearing harzburgites.

Our results indicate that P is more compatible in olivine than in pyroxenes, as $D_P^{Ol/Opx} = 8 \pm 2$, $D_P^{Ol/Cpx} = 1.9 \pm 0.2$, and $D_P^{Cpx/Opx} = 3 \pm 1$. These values broadly agree with previous xenolith data ($D_P^{Ol/Opx} = 2 \pm 2$, $D_P^{Ol/Cpx} = 1.0 \pm 0.1$, and $D_P^{Cpx/Opx} = 2 \pm 1$), given analytical uncertainties. Substitution of P into silicates can occur by the charge-coupled substitution $2\text{Si}^{4+} = \text{P}^{5+} + \text{Al}^{3+}$, but such a mechanism cannot explain the preference of P for

olivine over Al-bearing pyroxenes. Recent experimental work by Kohn & Grant (2013) has shown that the incorporation of P into olivine is not dependent on Al. Instead, they found that P substitutes for Si in olivine and is charge-balanced by Mg vacancies, implying that $D_P^{Ol/Opx}$ is controlled by the energetics of producing Mg vacancies. Clearly, more measurements of P in peridotites are necessary to better understand the behavior of this volatile element in the mantle.

7. Discussion of fluorine in peridotites

Results from this study also provide constraints on the behavior of F in peridotites. Concentrations of F range from 0.02 to 2 ppm in olivine, from 0.1 to 26 ppm in Opx and from 0.1 to 66 ppm in Cpx (Fig. 3). These values are in agreement with the range measured by Mosenfelder & Rossman (2013a, 2013b) for mantle xenoliths. Fluorine concentrations probably extend to lower values, as several samples were below detection. Converted to bulk rock concentrations, our samples have bulk F concentrations of 0.1-18 ppm. For comparison, the estimated concentration of F in the upper mantle is 11±5 ppm (Salters & Stracke, 2004) and in bulk silicate Earth is 25 ppm (McDonough & Sun, 1995). Samples with concentrations >11 ppm are Pali Aike xenoliths and SWIR pyroxenite veins, which are not necessarily expected to have low concentrations. In contrast, the amount of F in residual SWIR peridotites is <11 ppm, confirming that F is incompatible during melting.

Based on this study, F partition coefficients are $D_F^{Ol/Opx} = 0.06 \pm 0.05$ (N=5), $D_F^{Ol/Opx} = 0.02 \pm 0.02$ (N=4), and $D_F^{Cpx/Opx} = 3.5 \pm 1$ (N=17). A single experimental estimate of $D_F^{Ol/Opx} = 0.11 \pm 0.02$ from Beyer et al. (2012) provides a comparison. The value for $D_F^{Cpx/Opx}$ is reasonably robust, but the low concentration of F in olivine and the small number of

olivine analyses means that more data are necessary to improve estimates of $D_F^{Ol/Opx}$ and $D_F^{Ol/Cpx}$. Despite this, existing data indicate that the order of relative F compatibility is Cpx>Opx>Ol, which is the same order as for H₂O, but different than for P.

Several studies have suggested that F substitutes into NAMs via the same mechanisms as hydrogen (Hervig & Bell, 2005; Guggino et al., 2007; Bromiley & Kohn, 2007; O'Leary et al., 2010; Mosenfelder et al., 2011; Beyer et al., 2012; Dalou et al., 2012; Mosenfelder & Rossman, 2013a, 2013b). However, fluorine is also proposed to behave similarly to phosphorous during mantle melting (Schilling et al., 1980; Saal et al., 2002), with the relatively constant F/P ratio of MORBs being used to constrain upper mantle P (41 ppm; Salters & Stracke, 2004). This observation is surprising given that olivine is the main mantle host for P, whereas Cpx is the main host for F. Hence, more studies of F in peridotites and melts are necessary to constrain the amount of F in the mantle, particularly as recent work (e.g., Bromiley & Kohn, 2007; Beyer et al., 2012; Mosenfelder & Rossman, 2013a, 2013b) suggests that NAMs may control the mantle F budget.

If F and H_2O in olivine are correlated, then F contents in olivine could be used to calculate olivine H_2O concentrations. This type of analysis would provide confirmation of olivine H_2O concentrations calculated from pyroxene H_2O concentrations. More data for F and H_2O in undegassed olivines are necessary for this type of analysis to be possible.

8. Conclusions

This study presents data for volatile (H₂O, P and F) concentrations in olivine, orthopyroxene and clinopyroxene from abyssal, orogenic and xenolith peridotites. Our results demonstrate that pyroxenes can be used to constrain upper mantle water concentrations, but

that olivines in orogenic and abyssal peridotites have diffusively lost water. At high levels of alteration, pyroxenes show evidence for water enrichment, but this can largely be avoided by petrographic characterization of samples prior to analysis. If the partition coefficient D_{H2O}^{OllOpx} or D_{H2O}^{OllOpx} is known, the amount of water in upper mantle olivines can be determined from the water content of co-existing pyroxenes. The bulk water concentration for peridotites can then be calculated using mineral modes. Hence, the analysis of water in pyroxenes provides a powerful tool for investigating the role of water in upper mantle processes, such as melting and deformation.

The amount of water in Cpx in this study ranges from 60-670 ppm, with the lowest concentration occurring in an abyssal pyroxenite vein and the highest concentration in a Pali Aike xenolith. Opx ranges from 10-300 ppm, with the lowest water concentration also occurring in an abyssal pyroxenite vein and the highest concentration in a deformed Josephine peridotite. The average Cpx/Opx partition coefficient in this study is in close agreement with published xenolith values, which combined have a value of $D_{H2O}^{cpx/Opx} = 2.6 \pm 0.9 \ (152 \ \text{samples}). \ \text{However, natural samples are systematically offset from published experimental values} \ (D_{H2O}^{Cpx/Opx} = 1.3 \pm 0.3 \ , 10 \ \text{experiments}). \ \text{Possible causes for this offset include differences in composition, total water content, temperature and oxygen fugacity.}$

Olivine concentrations are calculated based on Opx water concentrations and using the experimental estimate of $D_{H2O}^{Ol/Opx}=0.11\pm0.03$, which gives an olivine concentration range of 1-34 ppm H₂O (16-550 ppm H/Si). Lithospheric effective viscosity, calculated from these olivine water concentrations and the dislocation creep flow law, is 6×10^{19} Pa s at

1250°C and 15 km depth for the most water-rich peridotite, compared to a dry effective viscosity of 2.5×10^{21} Pa s. At 1350°C and 100 km, the viscosity of the wettest peridotite is reduced to 1.5×10^{19} Pa s, compared to a dry viscosity of 2×10^{21} Pa s.

Calculated bulk rock water concentrations are 20-220 ppm, estimated using mineral concentrations and modes. Among abyssal peridotites, these concentrations are correlated with Cpx mode, bulk Al_2O_3 , bulk Ce and spinel Cr#, all of which are proxies for degree of melting. However, while modeling of fractional melting can reproduce observed REE patterns for ridge peridotites, it cannot reproduce the water contents. Abyssal peridotites thus appear to have higher water concentrations than expected for the residues of melting. One possible explanation for this is the addition of water by late-stage melt percolation, occurring at temperatures too low for other elements to diffusively equilibrate. Pyroxenites and pyroxenite-veined peridotites associated with Bouvet Hotspot have very low water contents and are best explained by the presence of recycled dehydrated oceanic crust in the plume source.

Phosphorous, which was only measured in a few samples, is more compatible in olivine than in pyroxenes, with concentrations of 50 ppm in olivine, 1-15 ppm in Opx and 5-29 ppm in Cpx. Fluorine concentrations are 0.02-2 ppm in olivine, 0.1-26 ppm in Opx and 0.1-66 ppm in Cpx. Calculated bulk F concentrations using mineral modes give a range of 0.1-18 ppm. Fluorine demonstrates similar partitioning behavior to H₂O in peridotites, but with lower concentrations. If F substitutes into olivine via the same mechanisms as H⁺, then it could be possible to determine original water contents in olivine based on F concentrations.

Acknowledgements

J. Wang is thanked for assistance with the SIMS analyses. C. MacLeod and H. Dick generously provided some of the abyssal peridotite samples. We thank S. Demouchy, G. Gaetani, M. Hirschmann, G. Hirth, C. Holyoke, J. O'Leary, P. Skemer, and E. Stolper for useful discussions. S. Kohn, T. Tenner, and H. Skogby gave insightful reviews and M. Walter provided thoughtful editorial handling. All new data presented in this paper are available in the 7 tables and 4 supplemental tables. This study was supported by Carnegie Institution of Washington and by NSF grant EAR-1255620 to JMW.

References

- Alt, J. C., W. C. Shanks, W. Bach, H. Paulick, C. J. Garrido, and G. Beaudoin (2007), Hydrothermal alteration and microbial sulfate reduction in peridotite and gabbro exposed by detachment faulting at the Mid-Atlantic Ridge, 15°20'N (ODP Leg 209): A sulfur and oxygen isotope study, *Geochemistry, Geophysics, and Geosystems*, 8(8), Q08002, doi:10.1029/2007GC001617.
- Amundsen, H. E. F., W. L. Griffin, and S. Y. O'Reilly (1987), The lower crust and upper mantle beneath northwestern Spitsbergen: evidence from xenoliths and geophysics, *Tectonophysics*, *139*, 169–185.
- Anders, E., and N. Grevesse (1989), Abundances of the elements: Meteoritic and solar, *Geochimica et Cosmochimica Acta*, 53(1), 197–214.
- Andrut, M., F. Brandstätter, and A. Beran (2003), Trace hydrogen zoning in diopside, *Mineralogy and Petrology*, 78, 231–241.
- Arai, S., and S. Ishimaru (2007), Insights into Petrological Characteristics of the Lithosphere of Mantle Wedge beneath Arcs through Peridotite Xenoliths: A Review, *Journal of Petrology*, 49(4), 665–695, doi:10.1093/petrology/egm069.
- Ardia, P., M. M. Hirschmann, A. C. Withers, and T. J. Tenner (2013), H₂O storage capacity of olivine at 5-8 GPa and consequences for dehydration partial melting of the upper mantle, *Earth and Planetary Science Letters*, 345-348, 104–116.
- Asimow, P. D., J. E. Dixon, and C. H. Langmuir (2004), A hydrous melting and fractionation model for mid-ocean ridge basalts: Application to the Mid-Atlantic Ridge near the Azores, *Geochemistry, Geophysics, Geosystems*, *5*(1), Q01E16, doi:10.1029/2003GC000568.
- Aubaud, C., A. C. Withers, M. M. Hirschmann, Y. Guan, L. A. Leshin, S. J. Mackwell, and D. R. Bell (2007), Intercalibration of FTIR and SIMS for hydrogen measurements in glasses and nominally anhydrous minerals, *American Mineralogist*, 92(5-6), 811–828,

- doi:10.2138/am.2007.2248.
- Aubaud, C., E. H. Hauri, and M. M. Hirschmann (2004), Hydrogen partition coefficients between nominally anhydrous minerals and basaltic melts, *Geophys. Res. Lett.*, *31*, L20611, doi:10.1029/2004GL021341.
- Aubaud, C., H. Bureau, C. Raepsaet, H. Khodja, A. C. Withers, M. M. Hirschmann, and D. R. Bell (2009), Calibration of the infrared molar absorption coefficients for H in olivine, clinopyroxene and rhyolitic glass by elastic recoil detection analysis, *Chemical Geology*, 262(1-2), 78–86, doi:10.1016/j.chemgeo.2009.01.001.
- Aubaud, C., M. M. Hirschmann, A. C. Withers, and R. L. Hervig (2008), Hydrogen partitioning between melt, clinopyroxene, and garnet at 3 GPa in a hydrous MORB with 6 wt.% H₂O, *Contributions to Mineralogy and Petrology*, 156(5), 607–625.
- Bach, W., and F. Klein (2009), The petrology of seafloor rodingites: Insights from geochemical reaction path modeling, *Lithos*, *112*(1-2), 103–117, doi:10.1016/j.lithos.2008.10.022.
- Bach, W., C. J. Garrido, H. Paulick, J. Harvey, and M. Rosner (2004), Seawater-peridotite interactions: First insights from ODP Leg 209, MAR 15°N, *Geochemistry, Geophysics, and Geosystems*, 5(9), Q09F26, doi:10.1029/2004GC000744.
- Bai, Q., and D. L. Kohlstedt (1992), Substantial hydrogen solubility in olivine and implications for water storage in the mantle, *Nature*, *357*, 672–674.
- Bell, D. R., and G. R. Rossman (1992), Water in Earth's mantle: The role of nominally anhydrous minerals, *Science*, *255*(5050), 1391–1397.
- Bell, D. R., G. R. Rossman, J. Maldener, D. Endisch, and F. Rauch (2003), Hydroxide in olivine: A quantitative determination of the absolute amount and calibration of the IR spectrum, *Journal of Geophysical Research*, 108(B2), 1–9, doi:10.1029/2001JB000679.
- Bell, D. R., P. D. Ihinger, and G. R. Rossman (1995), Quantitative analysis of trace OH in garnet and pyroxenes, *American Mineralogist*, 80(5), 465–474.
- Beyer, C., S. Klemme, M. Wiedenbeck, A. Stracke, and C. Vollmer (2012), Fluorine in nominally fluorine-free mantle minerals: Experimental partitioning of F between olivine, orthopyroxene and silicate melts with implications for magmatic processes, *Earth and Planetary Science Letters*, 337-338, 1–9, doi:10.1016/j.epsl.2012.05.003.
- Bloomer, S. H., and R. L. Fisher (1987), Petrology and Geochemistry of Igneous Rocks from the Tonga Trench A Non-Accreting Plate Boundary, *J. Geol.*, *95*, 469–495.
- Bonadiman, C., Y. Hao, M. Coltorti, L. Dallai, B. Faccini, Y. Huang, and Q.-K. Xia (2009), Water contents of pyroxenes in intraplate lithospheric mantle, *European Journal of Mineralogy*, 21(3), 637–647.
- Bromiley, D. W., and S. C. Kohn (2007), Comparisons between fluoride and hydroxide incorporation in nominally anhydrous and fluorine-free mantle minerals, *Goldschmidt Conference Abstracts*, 71, A124.
- Carpenter, S. (2003), The kinetics of hydrogen diffusion in single crystal orthopyroxene, PhD Thesis, Pennsylvania State University.
- Cherniak, D. J., and A. Dimanov (2010), Diffusion in Pyroxene, Mica and Amphibole, *Reviews in Mineralogy and Geochemistry*, 72, 641–690, doi:10.2138/rmg.2010.72.14.
- Cherniak, D. J., and Y. Liang (2007), Rare earth element diffusion in natural enstatite,

- Geochimica et Cosmochimica Acta, 71(5), 1324–1340, doi:10.1016/j.gca.2006.12.001.
- Craddock, P. R., J. M. Warren, and N. Dauphas (2013), Abyssal peridotites reveal the near-chondritic Fe isotopic composition of the Earth, *Earth and Planetary Science Letters*, 365, 63–76, doi:10.1016/j.epsl.2013.01.011.
- Dai, L., and S.-I. Karato (2009), Electrical conductivity of orthopyroxene: Implications for the water content of the asthenosphere, *Proc. Jpn. Acad., Ser. B*, 85(10), 466–475, doi:10.2183/pjab.85.466.
- Dalou, C., K. T. Koga, N. Shimizu, J. Boulon, and J.-L. Devidal (2011), Experimental determination of F and Cl partitioning between lherzolite and basaltic melt, *Contrib. Mineral. Petrol.*, *163*(4), 591–609, doi:10.1007/s00410-011-0688-2.
- De Hoog, J. C. M., L. Gall, and D. H. Cornell (2010), Trace-element geochemistry of mantle olivine and application to mantle petrogenesis and geothermobarometry, *Chemical Geology*, 270(1-4), 196–215, doi:10.1016/j.chemgeo.2009.11.017.
- Demouchy, S., and S. J. Mackwell (2006), Mechanisms of hydrogen incorporation and diffusion in iron-bearing olivine, *Phys. Chem. Minerals*, *33*(5), 347–355, doi:10.1007/s00269-006-0081-2.
- Demouchy, S., S. D. Jacobsen, F. Gaillard, and C. R. Stern (2006), Rapid magma ascent recorded by water diffusion profiles in mantle olivine, *Geol*, *34*(6), 429–432, doi:10.1130/G22386.1.
- Denis, C. M. M., S. Demouchy, and C. S. J. Shaw (2013), Evidence of dehydration in peridotites from Eifel Volcanic Field and estimates of the rate of magma ascent, *Journal of Volcanology and Geothermal Research*, 258, 85–99.
- Dick, H. J. B. (1976), Origin and emplacement of the Josephine Peridotite of southwestern Oregon, PhD Thesis, Yale University.
- Dixon, J. E., L. Leist, C. H. Langmuir, and J.-G. Schilling (2002), Recycled dehydrated lithosphere observed in plume-influenced mid-ocean-ridge basalt, *Nature*, 420, 385–389.
- Dyar, M. D., A. V. McGuire, and R. D. Ziegler (1989), Redox equilibria and crystal chemistry of coexisting minerals from spinel lherzolite mantle xenoliths, *American Mineralogist*, 74(9-10), 969–980.
- Eggins, S. M., R. L. Rudnick, and W. F. McDonough (1998), The composition of peridotites and their minerals: a laser-ablation ICP-MS study, *Earth and Planetary Science Letters*, 154, 53–71.
- Falus, G., A. Tommasi, J. Ingrin, and C. Szabo (2008), Deformation and seismic anisotropy of the lithospheric mantle in the southeastern Carpathians inferred from the study of mantle xenoliths, *Earth and Planetary Science Letters*, *272*(1-2), 50–64, doi:10.1016/j.epsl.2008.04.035.
- Farver, J. R. (2010), Oxygen and Hydrogen Diffusion in Minerals, *Reviews in Mineralogy and Geochemistry*, 72, 447–507, doi:10.2138/rmg.2010.72.10.
- Fisher, R. L., and C. G. Engel (1969), Ultramafic and basaltic rocks dredged from the nearshore flank of the Tonga trench, *Bulletin of the Geological Society of America*, 80, 1373–1378.
- Gaetani, G. A., and T. L. Grove (1998), The influence of water on melting of mantle peridotite, *Contrib. Mineral. Petrol.*, 131, 323–346.

- Godard, M., J.-L. Bodinier, and G. Vasseur (1995), Effects of mineralogical reactions on trace element redistributions in mantle rocks during percolation processes: A chromatographic approach, *Earth and Planetary Science Letters*, *133*, 449–461.
- Godard, M., Y. Lagabrielle, O. Alard, and J. Harvey (2008), Geochemistry of the highly depleted peridotites drilled at ODP Sites 1272 and 1274 (Fifteen-Twenty Fracture Zone, Mid-Atlantic Ridge): Implications for mantle dynamics beneath a slow spreading ridge, *Earth and Planetary Science Letters*, 267(3-4), 410–425, doi:10.1016/j.epsl.2007.11.058.
- Goetze, C., and D. L. Kohlstedt (1973), Laboratory study of dislocation climb and diffusion in olivine, *Journal of Geophysical Research*, 78(26), 5961–5971.
- Gose, J., E. Schmädicke, and A. Beran (2009), Water in enstatite from Mid-Atlantic Ridge peridotite: Evidence for the water content of suboceanic mantle? *Geol*, *37*(6), 543–546.
- Gose, J., E. Schmädicke, and R. Stalder (2011), Water in mantle orthopyroxene no visible change in defect water during serpentinization, *European Journal of Mineralogy*, 23(4), 529–536, doi:10.1127/0935-1221/2011/0023-2122.
- Grant, K. J., J. Ingrin, J.-P. Lorand, and P. Dumas (2007a), Water partitioning between mantle minerals from peridotite xenoliths, *Contrib. Mineral. Petrol.*, 154(1), 15–34, doi:10.1007/s00410-006-0177-1.
- Grant, K. J., S. C. Kohn, and R. A. Brooker (2006), Solubility and partitioning of water in synthetic forsterite and enstatite in the system MgO–SiO₂–H₂O±Al₂O₃, *Contrib. Mineral. Petrol.*, 151(6), 651–664.
- Grant, K. J., S. C. Kohn, and R. A. Brooker (2007b), The partitioning of water between olivine, orthopyroxene and melt synthesised in the system albite-forsterite-H₂O, *Earth and Planetary Science Letters*, 260(1-2), 227–241.
- Grant, T. B., and S. C. Kohn (2013), Phosphorus partitioning between olivine and melt: An experimental study in the system Mg₂SiO₄-Ca₂Al₂Si₂O₉-NaAlSi₃O₈-Mg₃(PO₄)₂, *American Mineralogist*, *98*, 1860–1869.
- Guggino, S. N., R. L. Hervig, and D. R. Bell (2007), Fluorine in Olivines from Plutonic, Extrusive, and Hypabyssal Suites, *Eos Transactions AGU*, 88(52), V41B–0609.
- Harper, G. D. (1984), The Josephine ophiolite, northwestern California, *Geol Soc America Bull*, 95(9), 1009–1026.
- Hauri, E. H., and S. R. Hart (1994), Constraints on melt migration from mantle plumes: A trace element study of peridotite xenoliths from Savai'i, Western Samoa, *Journal of Geophysical Research*, 99(B12), 24–301–24–321.
- Hauri, E. H., G. A. Gaetani, and T. H. Green (2006), Partitioning of water during melting of the Earth's upper mantle at H₂O-undersaturated conditions, *Earth and Planetary Science Letters*, 248, 715–734, doi:10.1016/j.epsl.2006.06.014.
- Hauri, E. H., J. Wang, J. E. Dixon, P. L. King, C. Mandeville, and S. Newman (2002), SIMS analysis of volatiles in silicate glasses 1. Calibration, matrix effects and comparisons with FTIR, *Chemical Geology*, 183, 99–114.
- Hauri, E. H., N. Shimizu, J. J. Dieu, and S. R. Hart (1993), Evidence for hotspot-related carbonatite metasomatism in the oceanic upper mantle, *Nature*, *365*, 221–227.
- Hellebrand, E., J. E. Snow, P. Hoppe, and A. W. Hofmann (2002), Garnet-field melting and late-stage refertilization in "residual" abyssal peridotites from the Central Indian Ridge, *Journal of Petrology*, *43*(12), 2305–2338.

- Hercule, S., and J. Ingrin (1999), Hydrogen in diopside: Diffusion, kinetics of extraction-incorporation, and solubility, *American Mineralogist*, 84, 1577–1587.
- Hervig, R. L., and D. R. Bell (2005), Fluorine and hydrogen in mantle megacrysts, *AGU Fall Meeting Abstracts*, *41*, V41A–1426.
- Hirschmann, M. M. (2006), Water, Melting, and the Deep Earth H₂O Cycle, *Annu. Rev. Earth. Planet. Sci.*, 34, 627–653.
- Hirth, G., and D. L. Kohlstedt (1996), Water in the oceanic upper mantle: implications for rheology, melt extraction and the evolution of the lithosphere, *Earth and Planetary Science Letters*, 144(1-2), 93–108.
- Hirth, G., and D. L. Kohlstedt (2003), Rheology of the upper mantle and the mantle wedge: A view from the experimentalists, *Geophysical Monograph*, 138, 83–105.
- Ingrin, J., and H. Skogby (2000), Hydrogen in nominally anhydrous upper-mantle minerals: concentration levels and implications, *European Journal of Mineralogy*, *12*, 543–570.
- Ingrin, J., and M. Blanchard (2006), Diffusion of Hydrogen in Minerals, *Reviews in Mineralogy and Geochemistry*, 62, 291–320.
- Ingrin, J., S. Hercule, and T. Charton (1995), Diffusion of hydrogen in diopside: Results of dehydration experiments, *Journal of Geophysical Research*, *100*(B8), 15489–15499.
- Ionov, D. A., C. Dupuy, S. Y. O'Reilly, M. G. Kopylova, and Y. S. Genshaft (1993), Carbonated peridotite xenoliths from Spitsbergen: implications for trace element signature of mantle carbonate metasomatism, *Earth and Planetary Science Letters*, 119(3), 283–297.
- Ionov, D. A., S. Y. O'Reilly, Y. S. Genshaft, and M. G. Kopylova (1996), Carbonate-bearing mantle peridotite xenoliths from Spitsbergen: phase relationships, mineral compositions and trace-element residence, *Contrib Mineral Petrol*, *125*(4), 375–392.
- Irving, A. J., and F. A. Frey (1984), Trace element abundances in megacrysts and their host basalts: Constraints on partition coefficients and megacryst genesis, *Geochimica et Cosmochimica Acta*, 48, 1201–1221.
- Jung, H., and S.-I. Karato (2001), Water-Induced Fabric Transitions in Olivine, *Science*, 293, 1460–1463.
- Jung, H., I. Katayama, Z. Jiang, T. Hiraga, and S.-I. Karato (2006), Effect of water and stress on the lattice-preferred orientation of olivine, *Tectonophysics*, *421*, 1–22, doi:10.1016/j.tecto.2006.02.011.
- Karato, S.-I. (2008), Deformation of Earth Materials, Cambridge University Press.
- Kelemen, P. B., and H. J. B. Dick (1995), Focused melt flow and localized deformation in the upper mantle: Juxtaposition of replacive dunite and ductile shear zones in the Josephine peridotite, SW Oregon, *Journal of Geophysical Research*, *100*(B1), 423–438.
- Kelemen, P. B., G. M. Yogodzinski, and D. W. Scholl (2003), Along-strike variation in the Aleutian island arc: Genesis of high Mg# andesite and implications for continental crust, in *The Subduction Factory*, vol. 138, edited by J. Eiler, pp. 223–276, American Geophysical Union.
- Kelemen, P. B., N. Shimizu, and V. J. M. Salters (1995), Extraction of mid-ocean-ridge basalt from the upwelling mantle by focused flow of melt in dunite channels, *Nature*, *375*, 747–753.

- Keppler, H., and N. Bolfan-Casanova (2006), Thermodynamics of water solubility and partitioning, *Reviews in Mineralogy and Geochemistry*, 62, 193–230.
- Kinzler, R. J. (1997), Melting of mantle peridotite at pressures approaching the spinel to garnet transition: Application to mid-ocean ridge basalt petrogenesis, *Journal of Geophysical Research*, 102(B1), 853–874.
- Klein, F., W. Bach, N. Jöns, T. M. McCollom, B. Moskowitz, and T. Berquó (2009), Iron partitioning and hydrogen generation during serpentinization of abyssal peridotites from 15°N on the Mid-Atlantic Ridge, *Geochimica et Cosmochimica Acta*, 73, 6868–6893, doi:10.1016/j.gca.2009.08.021.
- Kneller, E. A., P. E. van Keken, S.-I. Karato, and J. Park (2005), B-type olivine fabric in the mantle wedge: Insights from high-resolution non-Newtonian subduction zone models, *Earth and Planetary Science Letters*, 237, 781–797.
 - Koga, K. T., E. H. Hauri, M. M. Hirschmann, and D. R. Bell (2003), Hydrogen concentration analyses using SIMS and FTIR: Comparison and calibration for nominally anhydrous minerals, *Geochemistry, Geophysics, Geosystems*, *4*(2), Q01019, doi:10.1029/2002GC000378.
- Kohlstedt, D. L., and S. J. Mackwell (1998), Diffusion of Hydrogen and Intrinsic Point Defects in Olivine, *Zeitschrift fur physikalische Chemie*, 207, 147–162.
- Kohlstedt, D. L., and S. J. Mackwell (1999), Solubility and diffusion of 'water' in silicate minerals, in *Microscopic Properties and Processes in Minerals*, edited by K. Wright and R. Catlow, pp. 539–559, Kluwer Academic Publishers.
- Kohn, S. C., and K. J. Grant (2006), The Partitioning of Water Between Nominally Anhydrous Minerals and Silicate Melts, *Reviews in Mineralogy and Geochemistry*, 62, 231–241.
- Kohn, S. C., B. M. Roome, M. E. Smith, and A. P. Howes (2005), Testing a potential mantle geohygrometer; the effect of dissolved water on the intracrystalline partitioning of Al in orthopyroxene, *Earth and Planetary Science Letters*, 238, 342–350.
- Kovács, I., H. S. C. O'Neill, J. Hermann, and E. H. Hauri (2010), Site-specific infrared O-H absorption coefficients for water substitution into olivine, *American Mineralogist*, 95(2-3), 292–299, doi:10.2138/am.2010.3313.
- le Roux, P. J., S. B. Shirey, E. H. Hauri, M. R. Perfit, and J. F. Bender (2006), The effects of variable sources, processes and contaminants on the composition of northern EPR MORB (8-10°N and 12-14°N): Evidence from volatiles (H₂O, CO₂, S) and halogens (F, Cl), *Earth and Planetary Science Letters*, 251(3-4), 209–231, doi:10.1016/j.epsl.2006.09.012.
- Li, Z.-X. A., C.-T. A. Lee, A. H. Peslier, A. Lenardic, and S. J. Mackwell (2008), Water contents in mantle xenoliths from the Colorado Plateau and vicinity: Implications for the mantle rheology and hydration-induced thinning of continental lithosphere, *Journal of Geophysical Research*, 113(B09210), B09210, doi:10.1029/2007JB005540.
- Libowitzky, E., and G. R. Rossman (1997), An IR absorption calibration for water in minerals, *American Mineralogist*, 82(11), 1111–1115.
- Long, M. D., and P. G. Silver (2008), The subduction zone flow field from seismic anisotropy: A global view, *Science*, *319*(5861), 315–318.
- Mackwell, S. J., and D. L. Kohlstedt (1990), Diffusion of hydrogen in olivine: implications for water in the mantle, *Journal of Geophysical Research*, 95(B4), 5079–5088.

- Mallmann, G., H. S. C. O'Neill, and S. Klemme (2009), Heterogeneous distribution of phosphorus in olivine from otherwise well-equilibrated spinel peridotite xenoliths and its implications for the mantle geochemistry of lithium, *Contrib Mineral Petrol*, *158*(4), 485–504, doi:10.1007/s00410-009-0393-6.
- McDonough, W. F., and S.-S. Sun (1995), The composition of the Earth, *Chemical Geology*, 120(3-4), 223–253.
- Mei, S., and D. L. Kohlstedt (2000), Influence of water on plastic deformation of olivine aggregates: 2. Dislocation creep regime, *Journal of Geophysical Research*, 105(B9), 21471–21481, doi:10.1029/2000JB900180.
- Michael, P. J. (1995), Regionally distinctive sources of depleted MORB: Evidence from trace elements and H2O, *Earth and Planetary Science Letters*, *131*, 301–320.
 - Michael, P. J. et al. (2003), Magmatic and amagmatic seafloor generation at the ultraslow-spreading Gakkel ridge, Arctic Ocean, *Nature*, 423, 956–961.
 - Mosenfelder, J. L., and G. R. Rossman (2013a), Analysis of hydrogen and fluorine in pyroxenes: I. Orthopyroxene, *American Mineralogist*, *98*(5-6), 1026–1041, doi:10.2138/am.2013.4291.
 - Mosenfelder, J. L., and G. R. Rossman (2013b), Analysis of hydrogen and fluorine in pyroxenes: II. Clinopyroxene, *American Mineralogist*, *98*(5-6), 1042–1054, doi:10.2138/am.2013.4413.
 - Mosenfelder, J. L., M. Le Voyer, G. R. Rossman, Y. Guan, D. R. Bell, P. D. Asimow, and J. M. Eiler (2011), Analysis of hydrogen in olivine by SIMS: Evaluation of standards and protocol, *American Mineralogist*, *96*(11-12), 1725–1741, doi:10.2138/am.2011.3810.
 - Nadeau, S., P. Philippot, and F. C. C. O. Pineau (1993), Fluid inclusion and mineral isotopic compositions (HCO) in eclogitic rocks as tracers of local fluid migration during high-pressure metamorphism, *Earth and Planetary Science Letters*, *114*(4), 431–448, doi:10.1016/0012-821X(93)90074-J.
 - Nazzareni, S., H. Skogby, and P. F. Zanazzi (2010), Hydrogen content in clinopyroxene phenocrysts from Salina mafic lavas (Aeolian arc, Italy), *Contrib Mineral Petrol*, *162*(2), 275–288, doi:10.1007/s00410-010-0594-z.
 - Norman, M. D. (1998), Melting and metasomatism in the continental lithosphere: laser ablation ICPMS analysis of minerals in spinel lherzolites from eastern Australia, *Contrib Mineral Petrol*, 130(3), 240–255.
 - O'Leary, J. A., G. A. Gaetani, and E. H. Hauri (2010), The effect of tetrahedral Al³⁺ on the partitioning of water between clinopyroxene and silicate melt, *Earth and Planetary Science Letters*, 297(1-2), 111–120, doi:10.1016/j.epsl.2010.06.011.
 - Ohuchi, T., T. Kawazoe, Y. Nishihara, and T. Irifune (2012), Change of olivine a-axis alignment induced by water: Origin of seismic anisotropy in subduction zones, *Earth and Planetary Science Letters*, 317-318, 111–119, doi:10.1016/j.epsl.2011.11.022.
 - Ozawa, K., and N. Shimizu (1995), Open-system melting in the upper mantle: Constraints from the Hayachine-Miyamori ophiolite, northeastern Japan, *Journal of Geophysical Research*, 100(B11), 22315–22335.
 - Peslier, A. H. (2010), A review of water contents of nominally anhydrous natural minerals in the mantles of Earth, Mars and the Moon, *Journal of Volcanology and Geothermal Research*, 197(1-4), 239–258, doi:10.1016/j.jvolgeores.2009.10.006.

- Peslier, A. H., A. B. Woodland, and J. A. Wolff (2008), Fast kimberlite ascent rates estimated from hydrogen diffusion profiles in xenolithic mantle olivines from southern Africa, *Geochimica et Cosmochimica Acta*, 72(11), 2711–2722, doi:10.1016/j.gca.2008.03.019.
- Peslier, A. H., A. B. Woodland, D. R. Bell, M. Lazarov, and T. J. Lapen (2012), Metasomatic control of water contents in the Kaapvaal cratonic mantle, *Geochimica et Cosmochimica Acta*, 97, 213–246, doi:10.1016/j.gca.2012.08.028.
- Peslier, A. H., and J. F. Luhr (2006), Hydrogen loss from olivines in mantle xenoliths from Simcoe (USA) and Mexico: Mafic alkalic magma ascent rates and water budget of the sub-continental lithosphere, *Earth and Planetary Science Letters*, *242*, 302–319, doi:10.1016/j.epsl.2005.12.019.
- Peslier, A. H., J. F. Luhr, and J. Post (2002), Low water contents in pyroxenes from spinel-peridotites of the oxidized, sub-arc mantle wedge, *Earth and Planetary Science Letters*, 201, 69–86.
- Rauch, M., and H. Keppler (2002), Water solubility in orthopyroxene, *Contrib Mineral Petrol*, *143*(5), 525–536, doi:10.1007/s00410-002-0365-6.
- Saal, A. E., E. H. Hauri, C. H. Langmuir, and M. R. Perfit (2002), Vapour undersaturation in primitive mid-ocean-ridge basalt and the volatile content of the Earth's upper mantle, *Nature*, *419*(6906), 451–455, doi:10.1038/nature01073.
- Salters, V. J. M., and A. Stracke (2004), Composition of the depleted mantle, *Geochemistry*, *Geophysics*, and *Geosystems*, 5(5), doi:10.1029/2003GC000597.
- Schilling, J.-G., M. B. Bergeron, and R. Evans (1980), Halogens in the Mantle Beneath the North Atlantic, *Philosophical Transactions of the Royal Society of London. Series A: Mathematical, Physical and Engineering Sciences*, 297(1), 147–176, doi:10.1098/rsta.1980.0208.
- Schmädicke, E., J. Gose, and T. M. Will (2011), Heterogeneous mantle underneath the North Atlantic: Evidence from water in orthopyroxene, mineral composition and equilibrium conditions of spinel peridotite from different locations at the Mid-Atlantic Ridge, *Lithos*, 125(1-2), 308–320, doi:10.1016/j.lithos.2011.02.014.
- Shaw, A. M., M. D. Behn, S. E. Humphris, R. A. Sohn, and P. M. Gregg (2010), Deep pooling of low degree melts and volatile fluxes at the 85°E segment of the Gakkel Ridge: Evidence from olivine-hosted melt inclusions and glasses, *Earth and Planetary Science Letters*, 289(3-4), 311–322, doi:10.1016/j.epsl.2009.11.018.
- Skemer, P., J. M. Warren, L. N. Hansen, G. Hirth, and P. B. Kelemen (2013), The influence of water and LPO on the initiation and evolution of mantle shear zones, *Earth and Planetary Science Letters*, *375*, 222–233, doi:10.1016/j.epsl.2013.05.034.
- Skemer, P., J. M. Warren, P. B. Kelemen, and G. Hirth (2010), Microstructural and Rheological Evolution of a Mantle Shear Zone, *Journal of Petrology*, *51*(1-2), 43–53, doi:10.1093/petrology/egp057.
- Skogby, H. (2006), Water in Natural Mantle Minerals I: Pyroxenes, *Reviews in Mineralogy and Geochemistry*, 62(1), 155–167, doi:10.2138/rmg.2006.62.7.
- Skogby, H., D. R. Bell, and G. R. Rossman (1990), Hydroxide in pyroxene: Variations in the natural environment, *American Mineralogist*, 75(7-8), 764–774.
- Smith, G. P., D. A. Wiens, K. M. Fischer, L. M. Dorman, S. C. Webb, and J. A. Hildebrand

- (2001), A complex pattern of mantle flow in the Lau backarc, *Science*, 292(5517), 713–716, doi:10.1126/science.1058763.
- Stalder, R. (2004), Influence of Fe, Cr and Al on hydrogen incorporation in orthopyroxene, *European Journal of Mineralogy*, 16(5), 703–711, doi:10.1127/0935-1221/2004/0016-0703.
- Stalder, R., and H. Skogby (2002), Hydrogen incorporation in enstatite, *European Journal of Mineralogy*, *14*(6), 1139–1144.
- Stalder, R., and H. Skogby (2003), Hydrogen diffusion in natural and synthetic orthopyroxene, *Phys Chem Minerals*, *30*(1), 12–19, doi:10.1007/s00269-002-0285-z.
- Stalder, R., F. Prechtel, and T. Ludwig (2012), No site-specific infrared absorption coefficients for OH-defects in pure enstatite, *European Journal of Mineralogy*, 24, 465–470.
- Stalder, R., H. Purwin, and H. Skogby (2007), Influence of Fe on hydrogen diffusivity in orthopyroxene, *European Journal of Mineralogy*, *19*(6), 899–904, doi:10.1127/0935-1221/2007/0019-1780.
- Standish, J. J. (2006), The Influence of Ridge Geometry at the Ultraslow-Spreading Southwest Indian Ridge (9°-25°E): Basalt Composition Sensitivity to Variations in Source and Process, PhD Thesis, MIT/WHOI Joint Program.
- Standish, J. J., H. J. B. Dick, P. J. Michael, W. G. Melson, and T. O'Hearn (2008), MORB generation beneath the ultraslow spreading Southwest Indian Ridge (9–25°E): Major element chemistry and the importance of process versus source, *Geochemistry*, *Geophysics*, *Geosystems*, 9(5), 39, doi:10.1029/2008GC001959.
- Stern, C. R., R. Kilian, B. Olker, E. H. Hauri, and T. K. Kyser (1999), Evidence from mantle xenoliths for relatively thin (, *Lithos*, 48(1-4), 217–235.
- Stern, C. R., S. Saul, M. A. Skewes, and K. Futa (1989), Garnet peridotite xenoliths from the Pali-Aike alkali basalts of southernmost South America, *Geological Society of Australia Special Publication*, *14*, 735–744.
- Sundvall, R., and H. Skogby (2010), Hydrogen defect saturation in natural pyroxene, *Phys Chem Minerals*, 38(5), 335–344, doi:10.1007/s00269-010-0407-y.
- Sundvall, R., and R. Stalder (2011), Water in upper mantle pyroxene megacrysts and xenocrysts: A survey study, *American Mineralogist*, 96(8-9), 1215–1227, doi:10.2138/am.2011.3641.
- Sundvall, R., H. Skogby, and R. Stalder (2009), Dehydration-hydration mechanisms in synthetic Fe-poor diopside, *European Journal of Mineralogy*, 21(1), 17–26, doi:10.1127/0935-1221/2009/0021-1880.
- Tenner, T. J., M. M. Hirschmann, A. C. Withers, and P. Ardia (2012), H₂O storage capacity of olivine and low-Ca pyroxene from 10 to 13 GPa: consequences for dehydration melting above the transition zone, *Contrib Mineral Petrol*, 163, 297–316.
- Tenner, T. J., M. M. Hirschmann, A. C. Withers, and R. L. Hervig (2009), Hydrogen partitioning between nominally anhydrous upper mantle minerals and melt between 3 and 5 GPa and applications to hydrous peridotite partial melting, *Chemical Geology*, *262*(1-2), 42–56, doi:10.1016/j.chemgeo.2008.12.006.
- Van Orman, J. A., T. L. Grove, and N. Shimizu (2001), Rare earth element diffusion in diopside: influence of temperature, pressure, and ionic radius, and an elastic model for

- diffusion in silicates, Contrib Mineral Petrol, 141(6), 687–703.
- Vernières, J., M. Godard, and J.-L. Bodinier (1997), A plate model for the simulation of trace element fractionation during partial melting and magma transport in the Earth's upper mantle, *Journal of Geophysical Research*, 102(B11), 24771–24784.
- Wade, J. A., T. Plank, E. H. Hauri, K. A. Kelley, K. Roggensack, and M. Zimmer (2008), Prediction of magmatic water contents via measurement of H₂O in clinopyroxene phenocrysts, *Geol*, *36*(10), 799–802, doi:10.1130/G24964A.1.
- Warren, J. M. (2007), Geochemical and rheological constraints on the dynamics of the oceanic upper mantle, Massachusetts Institute of Technology and Woods Hole Oceanographic Institution, Woods Hole, MA.
- Warren, J. M., and S. B. Shirey (2012), Lead and osmium isotopic constraints on the oceanic mantle from single abyssal peridotite sulfides, *Earth and Planetary Science Letters*, *359*–360, 279–293, doi:10.1016/j.epsl.2012.09.055.
- Warren, J. M., G. Hirth, and P. B. Kelemen (2008), Evolution of olivine lattice preferred orientation during simple shear in the mantle, *Earth and Planetary Science Letters*, 272(3-4), 501–512, doi:10.1016/j.epsl.2008.03.063.
- Warren, J. M., N. Shimizu, C. Sakaguchi, H. J. B. Dick, and E. Nakamura (2009), An assessment of upper mantle heterogeneity based on abyssal peridotite isotopic compositions, *Journal of Geophysical Research*, *114*(B12203), B12203, doi:10.1029/2008JB006186.
- Withers, A. C. (2013), On the use of unpolarized infrared spectroscopy for quantitative analysis of absorbing species in birefringent crystals, *American Mineralogist*, 98(4), 689–697, doi:10.2138/am.2013.4316.
- Withers, A. C., and M. M. Hirschmann (2007), H₂O storage capacity of MgSiO₃ clinoenstatite at 8-13 GPa, 1,100-1,400°C, *Contrib Mineral Petrol*, 154, 663–674.
- Withers, A. C., H. Bureau, C. Raepsaet, and M. M. Hirschmann (2012), Calibration of infrared spectroscopy by elastic recoil detection analysis of H in synthetic olivine, *Chemical Geology*, 334, 92–98.
- Withers, A. C., M. M. Hirschmann, and T. J. Tenner (2011), The effect of Fe on olivine H₂O storage capacity: Consequences for H2O in the martian mantle, *American Mineralogist*, 96(7), 1039–1053, doi:10.2138/am.2011.3669.
- Witt-Eickschen, G., and H. S. C. O'Neill (2005), The effect of temperature on the equilibrium distribution of trace elements between clinopyroxene, orthopyroxene, olivine and spinel in upper mantle peridotite, *Chemical Geology*, *221*(1-2), 65–101, doi:10.1016/j.chemgeo.2005.04.005.
- Wolfe, C. J., and S. C. Solomon (1998), Shear-Wave Splitting and Implications for Mantle Flow Beneath the MELT Region of the East Pacific Rise, *Science*, *280*(5367), 1230–1232.
- Wood, B. J., L. T. Bryndzia, and K. E. Johnson (1990), Mantle oxidation state and its relationship to tectonic environment and fluid speciation, *Science*, 248(4953), 337–345.
- Woods, S. C., S. J. Mackwell, and M. D. Dyar (2000), Hydrogen in diopside: Diffusion profiles, *American Mineralogist*, 85(3-4), 480–487.
- Workman, R. K., and S. R. Hart (2005), Major and trace element composition of the depleted MORB mantle (DMM), *Earth and Planetary Science Letters*, 231(1-2), 53–72,

- doi:10.1016/j.epsl.2004.12.005.
- Wright, D. J., S. H. Bloomer, C. J. MacLeod, B. Taylor, and A. M. Goodlife (2000), Bathymetry of the Tonga Trench and Forearc: a map series, Marine Geophys. Res., 21, 489–511.
- Xia, Q.-Kl, Y. Hao, P. Li, E. Deloule, M. Coltorti, L. Dallai, X.-Z. Yang, and M. Feng (2010), Low water content of the Cenozoic lithospheric mantle beneath the eastern part of the North China Craton, Journal of Geophysical Research, 115(B7), B07207, doi:10.1029/2009JB006694.
- Yang, X.-Z., Q.-K. Xia, E. Deloule, L. Dallai, Q.-C. Fan, and M. Feng (2008), Water in minerals of the continental lithospheric mantle and overlying lower crust: A comparative study of peridotite and granulite xenoliths from the North China Craton, Chemical Geology, 256(1-2), 33-45.
- Yu. Y., X.-S. Xu, W. L. Griffin, S. Y. O'Reilly, and O.-K. Xia (2011), H₂O contents and their modification in the Cenozoic subcontinental lithospheric mantle beneath the Cathaysia block, SE China, *Lithos*, 126, 182–197.
- Zou, H. (1998), Trace element fractionation during modal and nonmodal dynamic melting and open-system melting: A mathematical treatment, Geochimica et Cosmochimica Acta, *62*(11), 1937–1945.

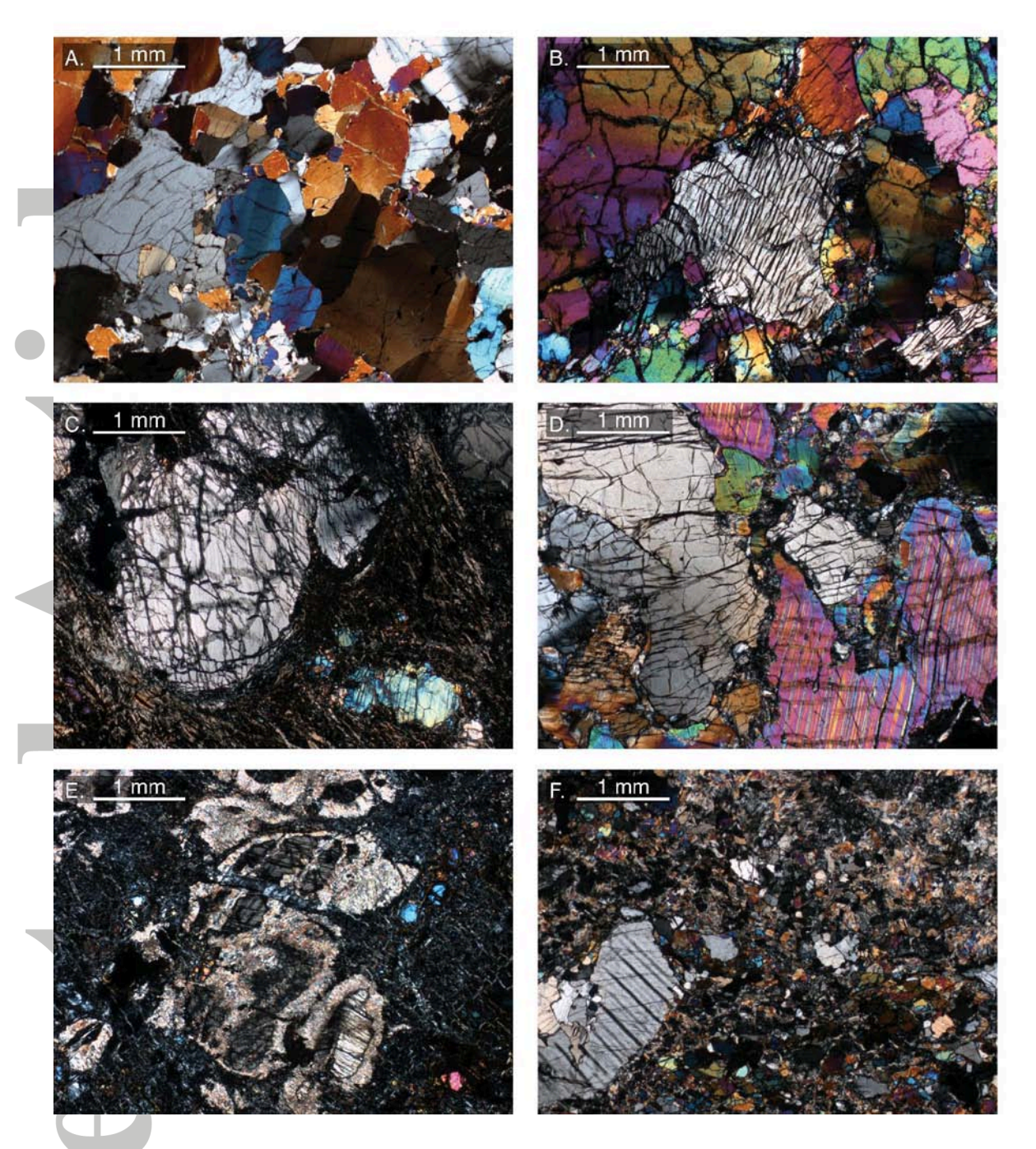


Figure 1. Photomicrographs of fresh and altered abyssal peridotites under cross-polarized light. **(A)** Tonga harzburgite BMRG08-98-2-1, fresh; **(B)** Gakkel harzburgite HLY0102-40-81, also fresh; **(C)** SWIR peridotite Van7-96-35, moderately altered; **(D)** SWIR pyroxenite vein Van7-96-09, low degree of alteration; **(E)** SWIR peridotite Van7-85-30, highly altered, with alteration coronas of amphibole around Opx; **(F)** SWIR pyroxenite vein Van7-96-16, highly altered, with fine-grained tremolite-serpentine groundmass replacing pyroxene.

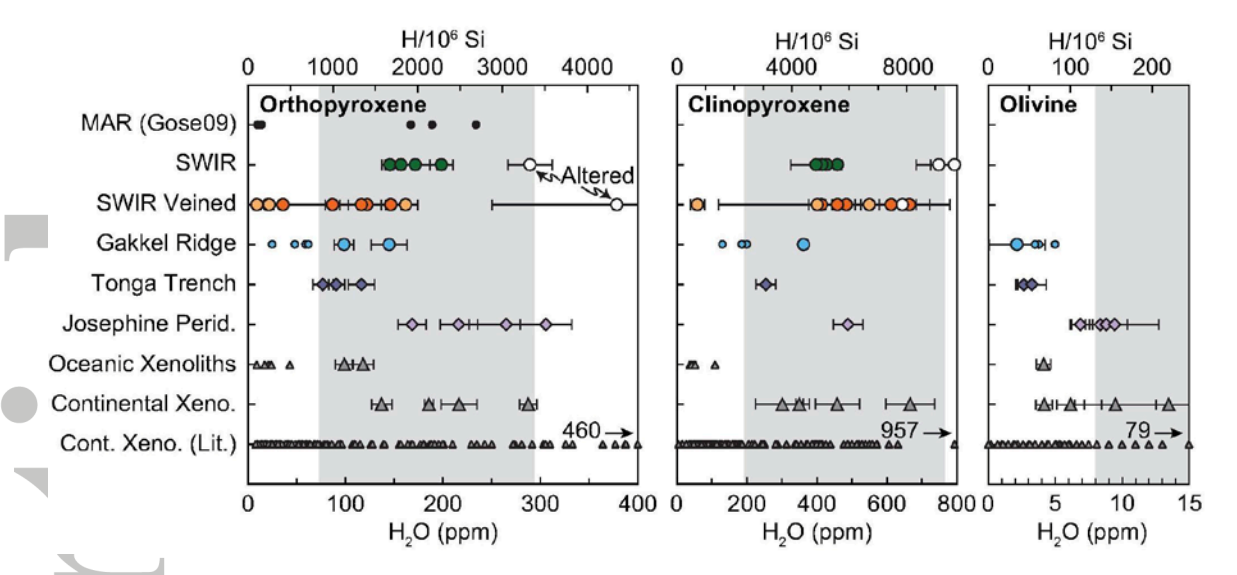


Figure 2. Ranges in water concentrations in peridotite NAMs. Larger symbols represent samples from this study and smaller symbols correspond to literature data. Error bars are 2σ standard deviations in the average of multiple analyses per sample. Three altered samples (see photomicrographs in Fig. 1) are shown as white symbols. "SWIR Veined" refers to dredge Van7-96, which consists of pyroxenite veins (light orange) and host peridotites (dark orange). Grey shaded fields indicate the estimated water concentration ranges of upper mantle minerals, calculated from bulk upper mantle water (50-200 ppm; Hirschmann, 2006), mineral modes (Workman & Hart, 2005) and mineral/mineral partition coefficients (see Table 3 for details). Literature data: Mid-Atlantic Ridge (MAR) abyssal peridotites from Gose et al. (2009) and Schmädicke et al. (2011); additional Gakkel peridotites from Peslier (2010); xenoliths from Bell & Rossman (1992), Peslier et al. (2002), Demouchy et al. (2006), Peslier & Luhr (2006), Aubaud et al. (2007), Grant et al. (2007b), Falus et al. (2008), Li et al. (2008), Yang et al. (2008), Bonadiman et al. (2009), Xia et al. (2010). Note that while xenoliths appear to extend to 0 ppm H₂O, the lowest concentration is 8 ppm in Opx, 5 ppm in Cpx and 0.2 ppm in olivine.



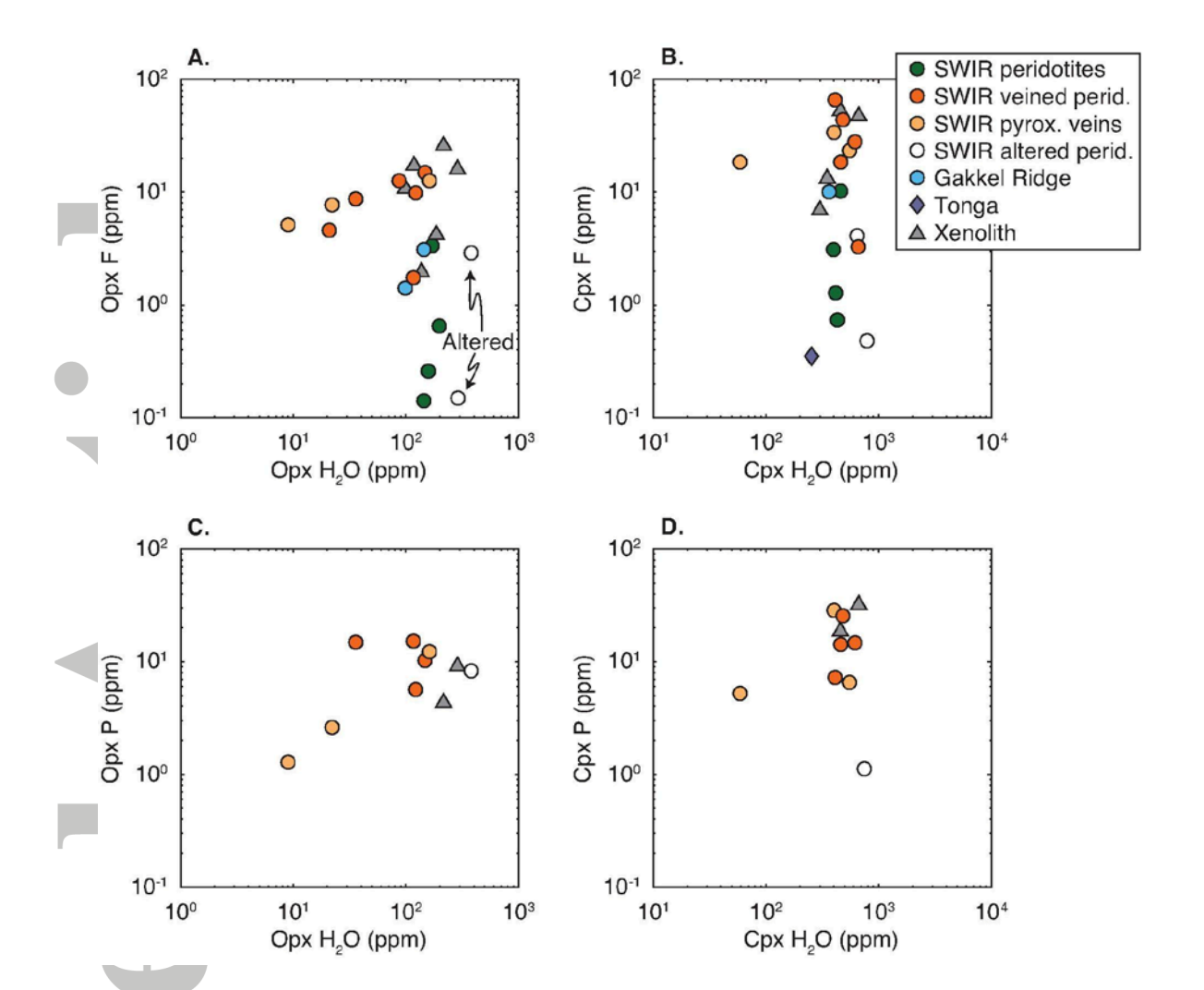


Figure 3. Variations in pyroxene F and P concentrations as a function of water concentrations. The fewer number of data points in C and D reflects the fact that P was only measured during the final analytical session.

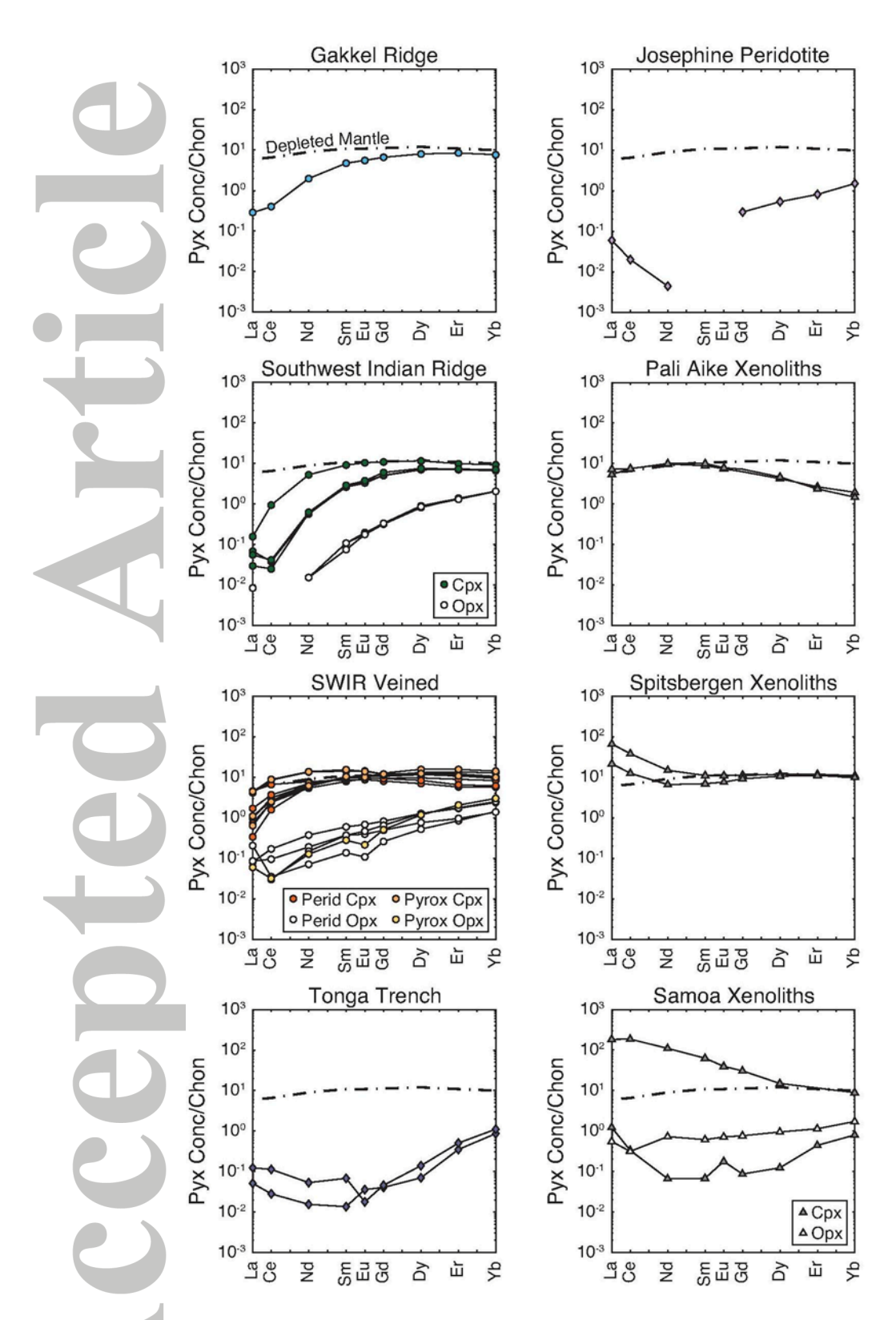


Figure 4. Plots of REE variations in peridotite Cpx and Opx; data are for Cpx unless noted in the legend. Data for SWIR samples are from Warren (2007) and Warren et al. (2009); data for Pali Aike xenoliths are from Hauri et al., (1993) and Hauri & Hart (1994); all other data

are from this study (Table 4). Concentrations are normalized to chondrite (Anders & Grevesse, 1989). The dashed line is the reference value for Cpx in the upper mantle before melting begins (depleted mantle or DM; Workman & Hart, 2005).

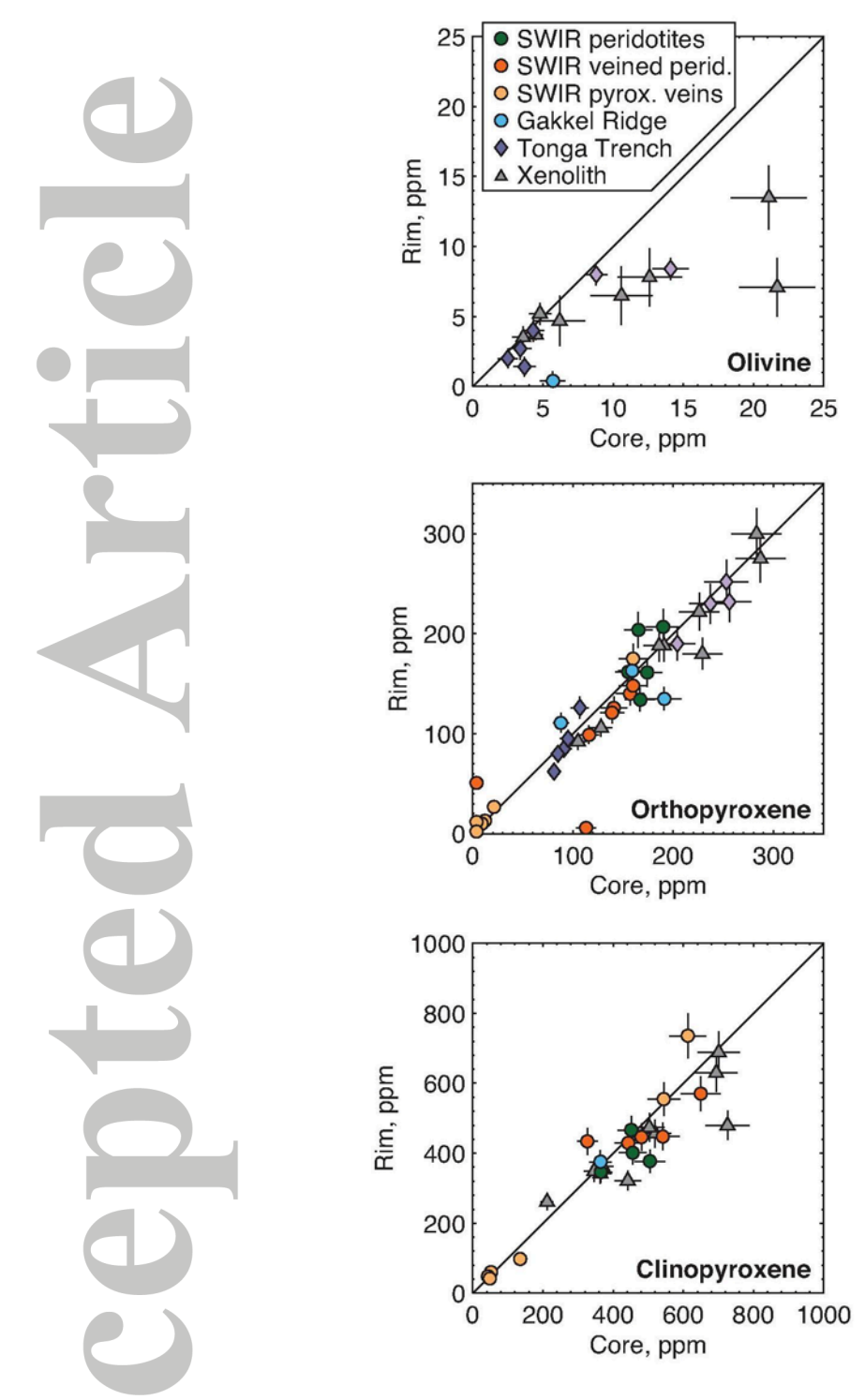


Figure 5. Paired core and rim water concentration analyses in individual grains. Most pyroxenes have similar core and rim concentrations, plotting within error of the 1:1 correspondence line. Olivine shows significant disequilibrium, with rims having lower concentrations.



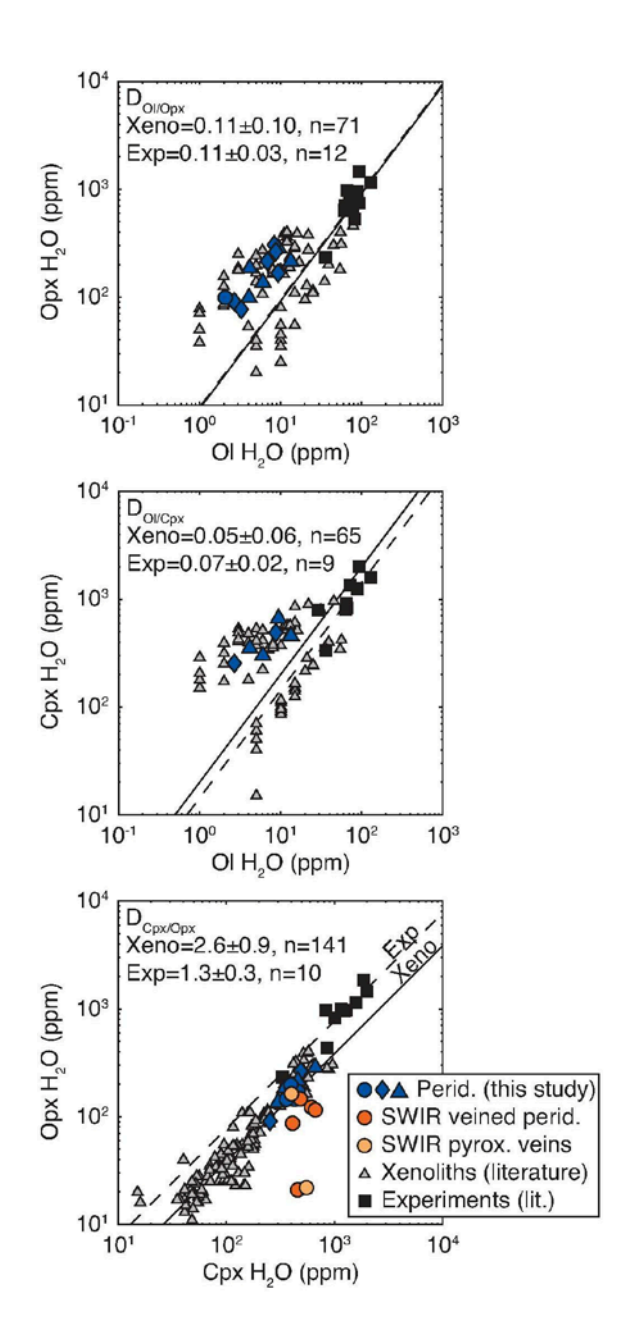


Figure 6. Co-variations of olivine, Opx, and Cpx water concentrations, compared to literature data for xenoliths (see references in Fig. 2) and experiments (Aubaud et al., 2004, 2008; Hauri et al., 2006; Tenner et al., 2009; O'Leary et al., 2010). Circles indicate ridge peridotites, diamonds indicate subduction peridotites and triangles indicate xenoliths. The lines represent regressions for $D_{H2O}^{Ol/Opx}$, $D_{H2O}^{Ol/Cpx}$, and $D_{H2O}^{Cpx/Opx}$ based on alumina-bearing low-pressure experimental data (dashed lines) and xenolith data (solid lines). Average values for the xenolith partition coefficients do not include samples from this study.

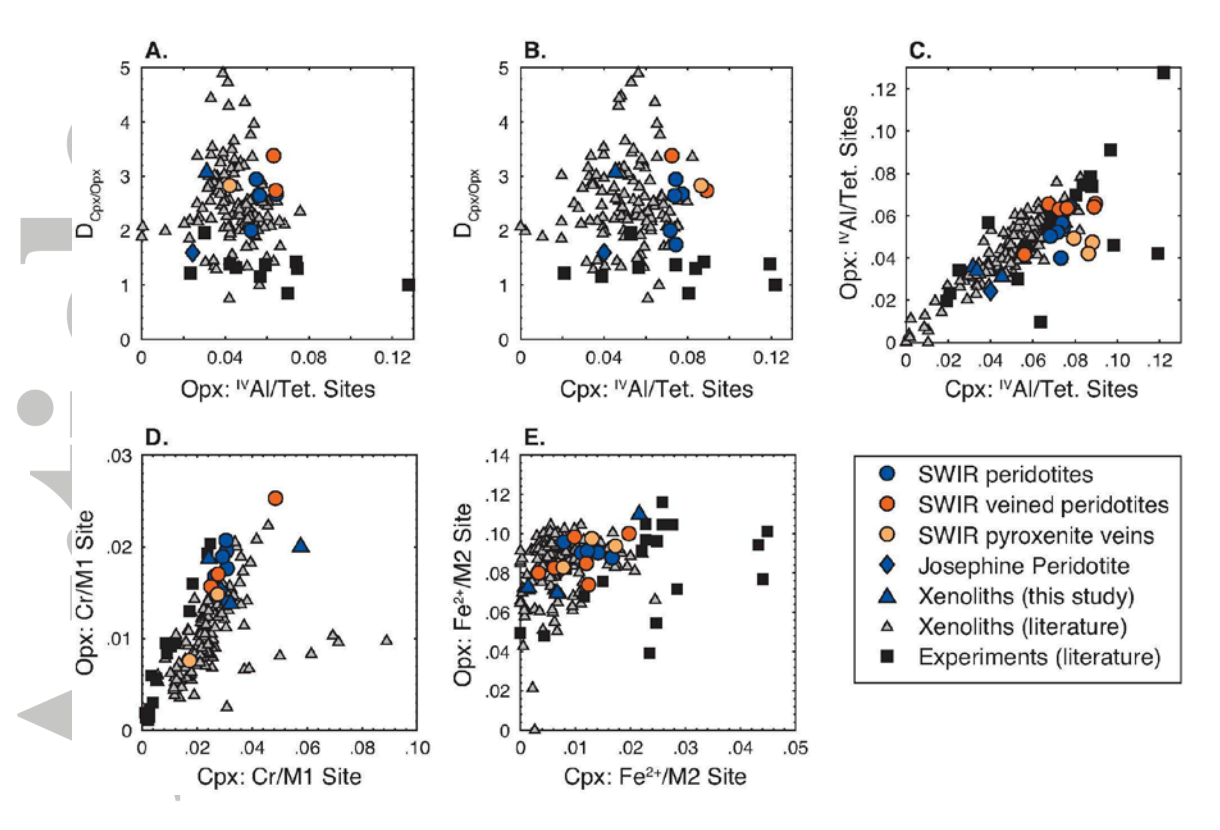


Figure 7. (A) Variation of $D_{H2O}^{Cpx/Opx}$ as a function of $^{IV}Al^{3+}$ content in Opx. Experiments show a weak partition coefficient dependence on $^{IV}Al^{3+}$, whereas natural samples do not. **(B)** Variation of $D_{H2O}^{Cpx/Opx}$ as a function of $^{IV}Al^{3+}$ content in Cpx. Systematic variations do not occur among experiments or natural samples. **(C)** Variation in $^{IV}Al^{3+}$ as a proportion of the pyroxene tetrahedral sites. Experiments and natural samples have similar amounts of $^{IV}Al^{3+}$ in both Opx and Cpx. Other cations (e.g., Ti^{4+} , Fe^{3+}) show similar variations. **(D)** Variation in Cr^{3+} as a proportion of the M1 site. Experiments have relatively more Cr^{3+} in Opx compared to Cpx. **(E)** Variation in Fe^{2+} as a proportion of the M2 site. Experiments have relatively less Fe^{2+} in Opx compared to Cpx. Mineral microprobe data for our samples are from Stern et al. (1989), Hauri & Hart (1994), Warren et al. (2009), and Skemer et al. (2010). Site occupancies were calculated from microprobe data assuming perfect stoichiometry, with data and calculated components provided in supplemental Table S4. References for literature data are in Fig. 2 for xenoliths and Fig. 6 for experiments.



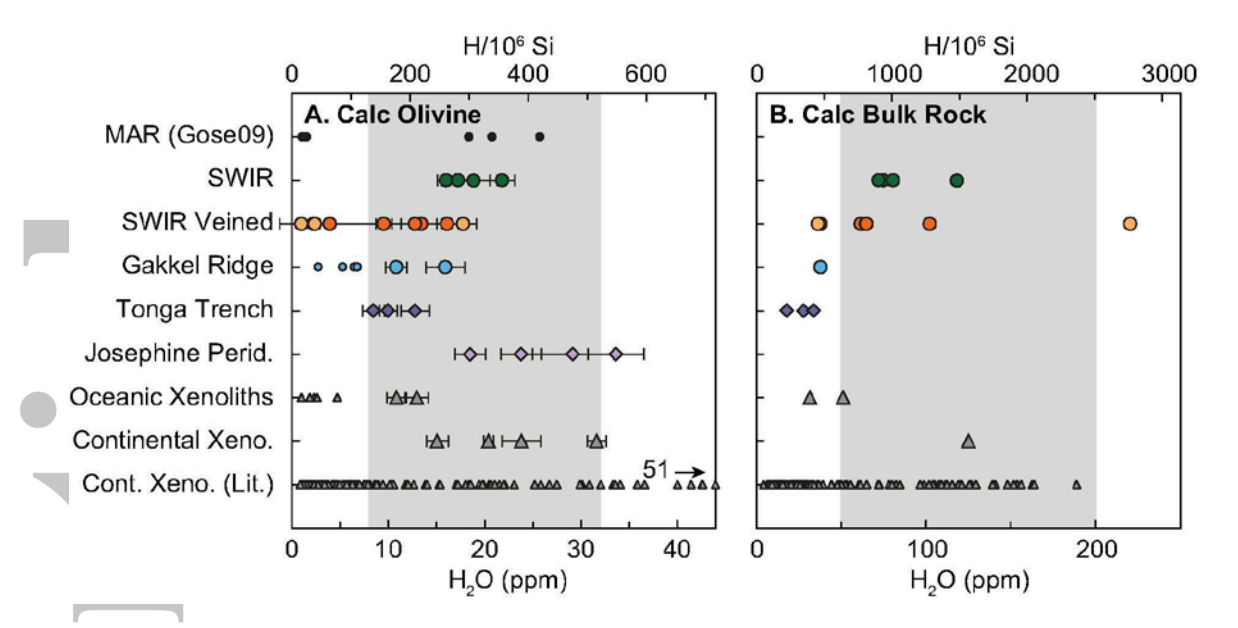


Figure 8. (A) Calculated water concentrations in olivine, based on Opx water concentrations and assuming $D_{H2O}^{Ol/Opx}$ =0.11. Error bars indicate 2 σ standard deviations in the average of multiple analyses per sample. (B) Calculated bulk peridotite water concentrations for samples that have measured mineral modes. Smaller symbols indicate literature data (see Fig. 2 for references). Grey shaded fields represent the estimated water concentration ranges in the upper mantle (see Table 3 for details).

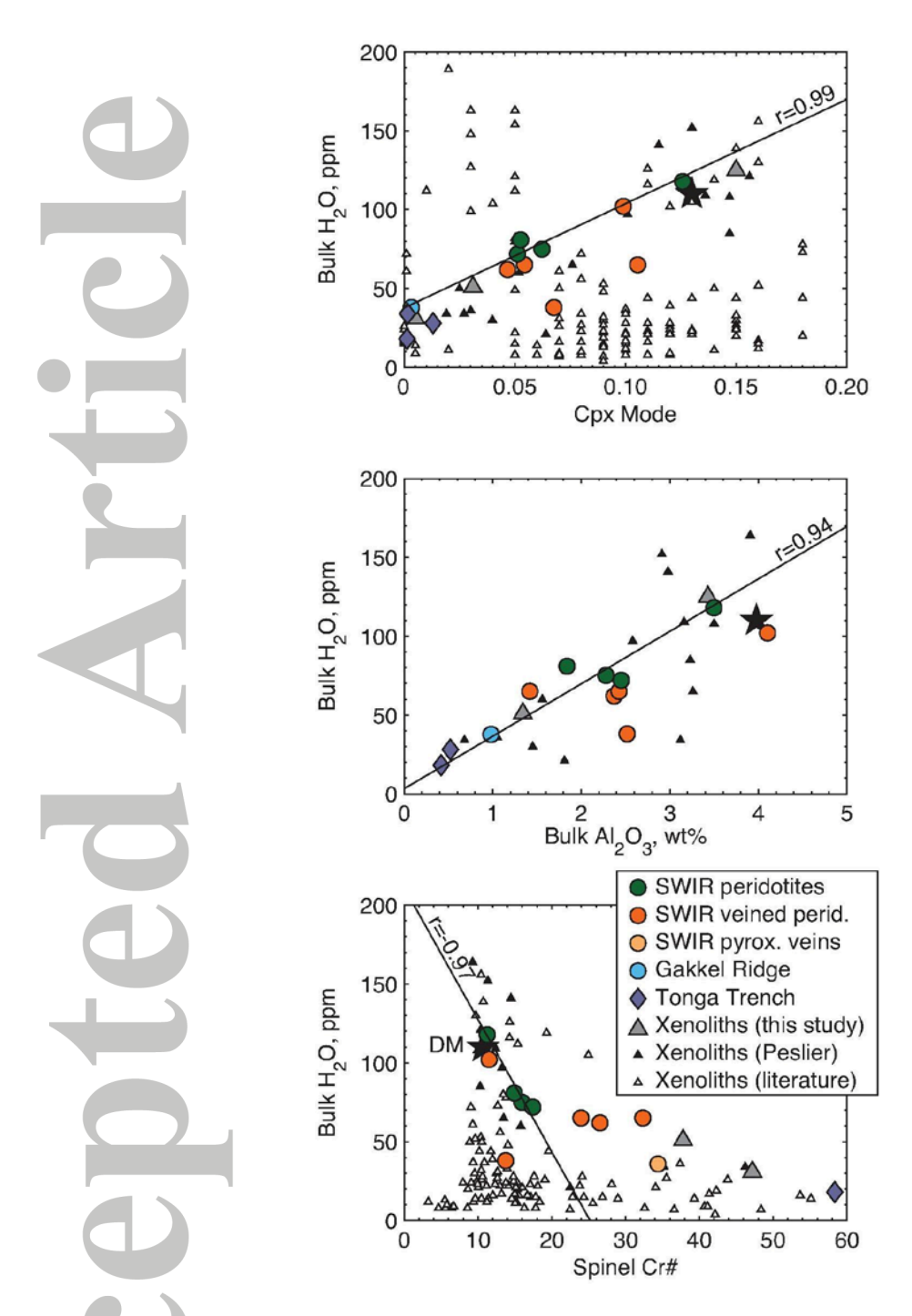


Figure 9. Variations in bulk peridotite water concentrations as a function of peridotite proxies for degree of melting. Solid lines are least squares regressions through the unveined ridge peridotites in this study, for which Cpx mode, bulk Al₂O₃ and spinel Cr# are given in Table 6. References for literature xenoliths are given in Fig. 2. The model composition of the source depleted mantle (DM, black star) is from Workman & Hart (2005).

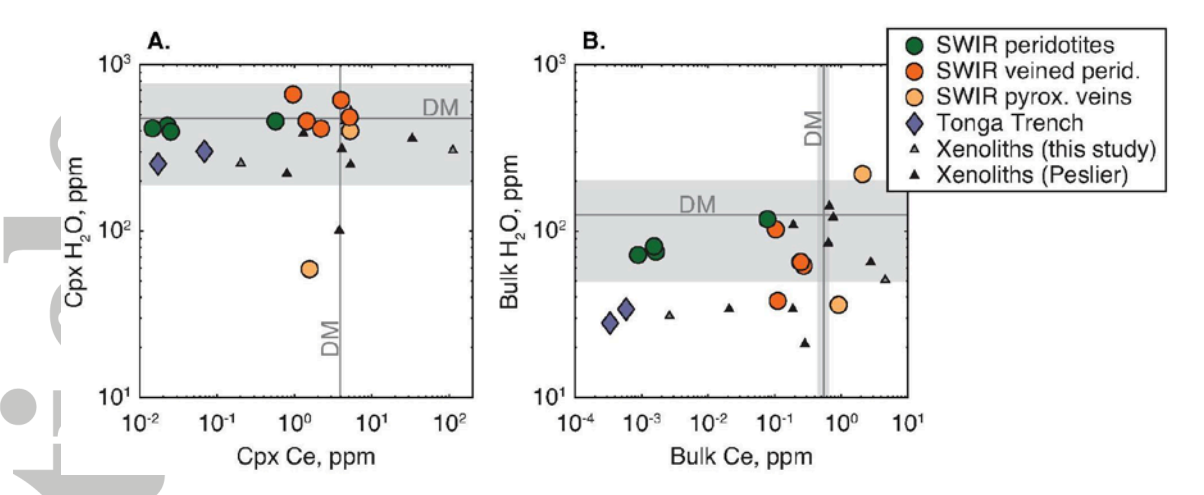


Figure 10. (A) Variation of measured water concentrations in Cpx compared to measured Cpx Ce concentrations. (B) Variation of calculated bulk H_2O concentrations as a function of calculated bulk Ce concentrations. For comparison, data from the xenolith study by Peslier et al. (2002) are shown. Bulk Ce concentrations are calculated from measured Cpx Ce concentrations using mineral modes (Table 6) and Ce mineral/melt partition coefficients (Table 7). The average estimated concentrations of upper mantle H_2O (Hirschmann, 2006) and Ce (Workman & Hart, 2005) are shown as grey lines, with the grey boxes indicating the ranges of these estimates. The concentration of H_2O in upper mantle Cpx (190-760 ppm) is calculated from the bulk mantle estimate (see Table 3 for details).



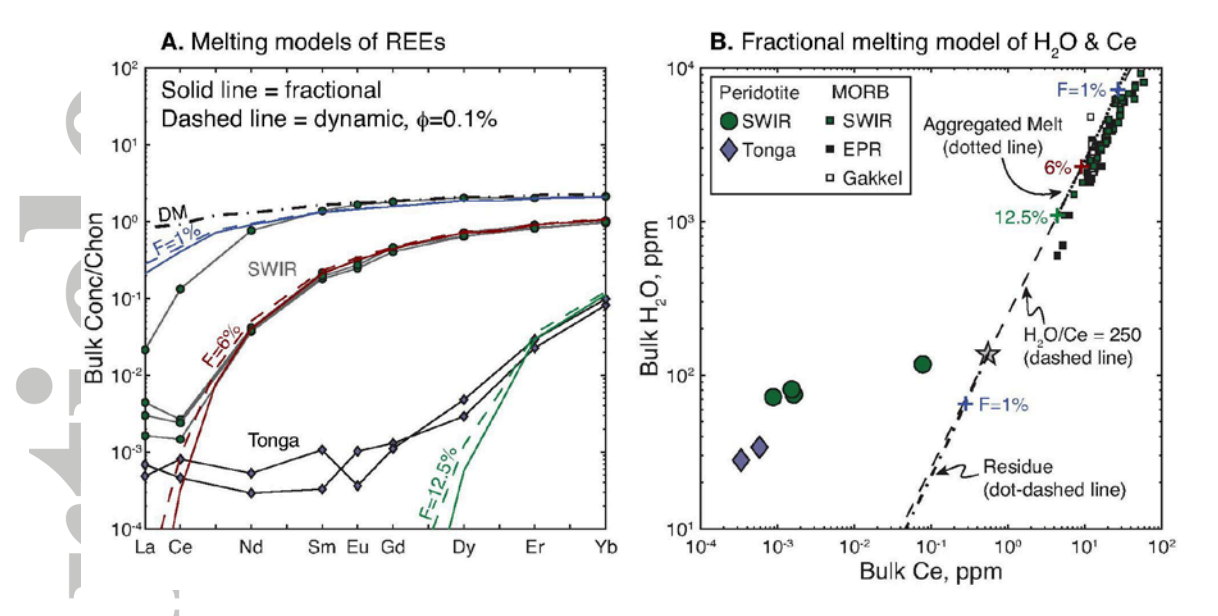


Figure 11. (A) Results of REE modeling of spinel field melting for bulk rock abyssal peridotites. Fractional and dynamic nonmodal melting models give similar results; for simplicity only the fractional melting model is shown in B. **(B)** The evolution of peridotite residue and aggregated melt for Ce and H₂O during fractional melting, using partition coefficients given in Table 7. Also shown are published H₂O-Ce datasets for MORBs (le Roux et al., 2006; Standish, 2006; Standish et al., 2008; Shaw et al., 2010). The melting model fits the basalt data (dotted line), but completely misses the peridotite data (dot-dashed line). In addition, the basalt data align along a line of constant H₂O-Ce ratio (dashed line), whereas the peridotite data plot far from this line.

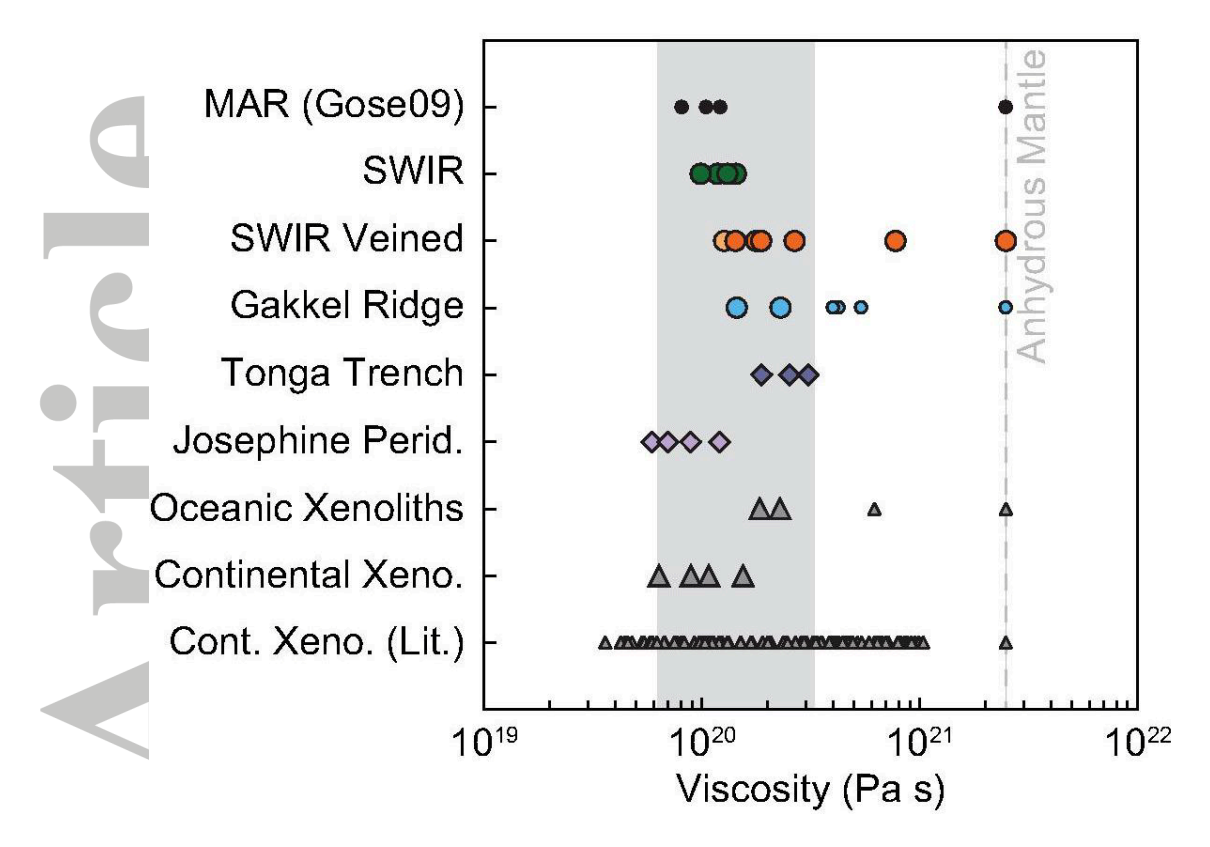


Figure 12. Range of effective mantle viscosities (Table 6), calculated at a temperature of 1250° C, pressure of 0.5 GPa (~ 15 km) and shear stress of 0.3 MPa. The dislocation creep flow law for wet olivine as a function of C_{OH} (Hirth & Kohlstedt, 2003) was used, combined with modeled olivine water concentrations (Table 6). At water contents < 3 ppm H_2O (< 50 ppm H/Si), the flow law for dry olivine was used to calculate viscosity, as creep rate is no longer controlled by the charge neutrality condition (Mei & Kohlstedt, 2000). The grey shaded box is the estimated viscosity range for the upper mantle based on the Hirschmann (2006) estimate for upper mantle water contents of 50-200 ppm H_2O (130-520 ppm H/Si) in olivine.

Table 1: Sample locations and types.

| | | | | Phases |
|--------------|----------------------------------|--------------------------|------------------|----------------|
| Sample | Location | Lithology | Alteration | analyzed |
| | | | | |
| D000 0 00 | | Peridotites | NA - d - a - 6 - | 0 |
| PS86-6-38 | SWIR, -52.35°S, 13.13°E | Lherzolite | Moderate | Opx, Cpx |
| Van7-85-30 | SWIR, -52.25°S, 15.23°E | Harzburgite | High | Орх |
| Van7-85-42 | SWIR, -52.25°S, 15.23°E | Lherzolite | Moderate | Opx, Cpx |
| Van7-85-47 | SWIR, -52.25°S, 15.23°E | Lherzolite | Moderate | Opx, Cpx |
| Van7-85-49 | SWIR, -52.25°S, 15.23°E | Lherzolite | Moderate | Opx, Cpx |
| Van7-86-27 | SWIR, -52.13°S, 15.15°E | Lherzolite Pyroxenite | High | Срх |
| Van7-96-09V | SWIR, -53.14°S, 9.98°E | Vein | Low | Орх, Срх |
| vani oo oo v | 377117, 33.11 3, 3.33 E | Pyroxenite | Moderate/Hig | ορλ, ορλ |
| Van7-96-16V | SWIR, -53.14°S, 9.98°E | Vein | h | Орх, Срх |
| r | | Perid w/ Pyx | | 1 / 1 |
| Van7-96-18M | SWIR, -53.14°S, 9.98°E | Vn | Moderate | Орх |
| | | Pyx Vn in | | |
| Van7-96-18V | SWIR, -53.14°S, 9.98°E | Perid | Moderate | Орх, Срх |
| \/7.00.04N4 | 0.4400 0.0005 | Harz w/ Pyx | NA - d - a - 4 - | 0 |
| Van7-96-21M | SWIR, -53.14°S, 9.98°E | Vn Dvy Vn in | Moderate | Орх, Срх |
| Van7-96-21V | SWIR, -53.14°S, 9.98°E | Pyx Vn in Harz | Moderate | Орх, Срх |
| Van7-96-25 | SWIR, -53.14°S, 9.98°E | Lherzolite | Moderate | Opx, Opx |
| Van7-96-28 | SWIR, -53.14°S, 9.98°E | Lherzolite | Moderate | Opx, Cpx |
| Van7-96-35 | SWIR, -53.14°S, 9.98°E | Lherzolite | Moderate | Opx, Cpx |
| Van7-96-38 | SWIR, -53.14°S, 9.98°E | Lherzolite | Moderate | Орх, Срх |
| HLY0102-40- | 3VIIX, -33.14 3, 9.90 L | Literzonite | Moderate | Орх, Орх |
| 81 | Gakkel Ridge, 85.45°N, 14.56°E | Harzburgite | Fresh | Oliv, Opx |
| PS59-235-17 | Gakkel Ridge, 84.66°N, 4.20°E | Lherzolite | Fresh | Орх, Срх |
| | Tonga Trench, -20.25°S, | | | - |
| 7TOW-57-4 | 173.42°W | Harzburgite | Fresh | Oliv, Opx, Cpx |
| BMRG08-98- | Tonga Trench, -19.25°S, | | | |
| 2-1 | 172.94°W | Harzburgite | Fresh | Oliv, Opx |
| 110141-00 14 | Tonga Trench, -20.38°S, | | | • |
| NOVA-88-A1 | 173.27°W | Harzburgite | Fresh | Орх |
| | Xeno | oliths | | |
| | Pali Aike volcanic field, | , mano | | |
| LS-33 | Patagonia | Gt Lherz | Fresh | Oliv, Opx, Cpx |
| | Pali Aike volcanic field, | | | |
| TMO | Patagonia | Gt-Sp Lherz | Fresh | Oliv, Opx, Cpx |
| SAV-AS1 | Sverrejfell Volcano, Spitsbergen | Lherzolite | Fresh | Oliv, Opx, Cpx |
| SAV-AS2 | Sverrejfell Volcano, Spitsbergen | Lherzolite | Fresh | Oliv, Opx, Cpx |
| SA-3-9 | Savai'i Island, Samoa | Harzburgite | Fresh | Oliv, Opx |
| SAV-1-28 | Savai'i Island, Samoa | Harzburgite | Fresh | Орх |
| | Orogenia | Doridotito | | |
| 2022 104 | _ | Peridotite | Modorata | Oliv Ony |
| 3923J01 | Josephine Peridotite, Oregon | Harzburgite | Moderate | Oliv, Opx |
| 3924J08 | Josephine Peridotite, Oregon | Harzburgite | Moderate | Oliv, Opx |
| 3925G01 | Josephine Peridotite, Oregon | Harzburgite | Moderate | Oliv, Opx |
| JP08PS01 | Josephine Peridotite, Oregon | Harzburgite | Moderate | Oliv, Opx, Cpx |

Table 2: Water concentrations in peridotite minerals.^a

| | | • | on Lithology Grains | | | H_2 | 0 | H | /Si | F^b | | P^{c} | |
|-----------------------------|----------|--------------|---------------------|--------|-----|-------|-----|------|------|--------|------|---------|-----|
| Sample | Type | Location | Lithology | Grains | Pts | ppm | ± | ppm | ± | ppm | ± | ppm | ± |
| _ | | | | | | | | | | | | | |
| HI V0102 | | | Olivine | | | | | | | | | | |
| HLY0102- 40-81 | Abyssal | Gakkel | Harzburgite | 1 | 7 | 2 | 2 | 35 | 34 | 0.04 | 0.02 | | |
| 7TOW-57-4 | Abyssal | Tonga Trench | Harzburgite | 2 | 4 | 2.7 | 0.6 | 43 | 10 | < 0.01 | 0.02 | | |
| BMRG08- | Hoyssur | ronga rrenen | Tiaizoaigite | _ | | 2.7 | 0.0 | .5 | 10 | 0.01 | | | |
| 98-2-1 | Abyssal | Tonga Trench | Harzburgite | 2 | 12 | 3 | 1 | 53 | 17 | < 0.01 | | | |
| LS-33 | Xenolith | Pali Aike | Gt Lherz | 2 | 11 | 13 | 5 | 220 | 82 | 1.3 | 0.2 | 39 | 2 |
| TMO | Xenolith | Pali Aike | Gt-Sp Lherz | 2 | 8 | 9 | 3 | 155 | 49 | 2.28 | 0.07 | 57 | 1 |
| SAV-AS1 | Xenolith | Spitsbergen | Lherzolite | 2 | 7 | 4.2 | 0.6 | 68 | 10 | 0.20 | 0.02 | | |
| SAV-AS2 | Xenolith | Spitsbergen | Lherzolite | 2 | 4 | 6 | 1 | 100 | 17 | 0.02 | 0.01 | | |
| SA-3-9 | Xenolith | Samoa | Harzburgite | 1 | 2 | 4.1 | 0.5 | 67 | 9 | 0.10 | 0.04 | | |
| 3923J01 | Orogenic | Josephine | Harzburgite | 2 | 4 | 9 | 3 | 154 | 54 | < 0.01 | | | |
| 3924J08 | Orogenic | Josephine | Harzburgite | 2 | 4 | 6.9 | 0.7 | 112 | 11 | < 0.01 | | | |
| 3925G01 | Orogenic | Josephine | Harzburgite | 1 | 2 | 8.4 | 0.5 | 137 | 9 | < 0.01 | | | |
| JP08PS01 | Orogenic | Josephine | Harzburgite | 3 | 4 | 9 | 2 | 144 | 26 | < 0.01 | | | |
| | | | | | | | | | | | | | |
| | | | Orthopyroxene | | | | | | | | | | |
| PS86-6-38 | Abyssal | SWIR | Lherzolite | 2 | 4 | 171 | 22 | 1971 | 252 | 3.4 | 0.2 | | |
| Van7-85-30 | Abyssal | SWIR | Harzburgite | 2 | 4 | 289 | 23 | 3327 | 263 | 0.15 | 0.04 | | |
| Van7-85-42 | Abyssal | SWIR | Lherzolite | 2 | 3 | 145 | 8 | 1672 | 91 | 0.14 | 0.04 | | |
| Van7-85-47 | Abyssal | SWIR | Lherzolite | 2 | 5 | 157 | 16 | 1804 | 184 | 0.26 | 0.03 | | |
| Van7-85-49 | Abyssal | SWIR | Lherzolite | 1 | 2 | 198 | 12 | 2282 | 135 | 0.65 | 0.00 | | |
| Van7-96- 09V | Abyssal | SWIR | Pyroxenite Vein | 4 | 10 | 9 | 4 | 105 | 48 | 5 | 1 | 1.3 | 0.5 |
| Van7-96- 16V Van7-96- | Abyssal | SWIR | Pyroxenite Vein | 4 | 8 | 378 | 128 | 4348 | 1467 | 3 | 3 | 8 | 6 |
| 18M Van7-96- | Abyssal | SWIR | Perid w/ Pyx Vn | 2 | 5 | 36 | 48 | 411 | 546 | 9 | 1 | 15 | 4 |
| 18V Van7-96- | Abyssal | SWIR | Pyx Vn in Perid | 1 | 4 | 22 | 5 | 251 | 52 | 8 | 2 | 2.6 | 0.2 |
| 21M Van7-96- | Abyssal | SWIR | Harz w/ Pyx Vn | 4 | 6 | 147 | 10 | 1685 | 116 | 15 | 6 | 10 | 2 |
| 21V | Abyssal | SWIR | Pyx Vn in Harz | 1 | 3 | 162 | 12 | 1860 | 140 | 12.6 | 0.9 | 12 | 1 |
| Van7-96-25 | Abyssal | SWIR | Lherzolite | 2 | 2 | 21 | 13 | 237 | 144 | 5 | 1 | | |
| Van7-96-28 | Abyssal | SWIR | Lherzolite | 4 | 7 | 122 | 19 | 1404 | 221 | 10 | 4 | 5.6 | 0.4 |
| Van7-96-35 | Abyssal | SWIR | Lherzolite | 1 | 1 | 87 | 8 | 998 | 88 | 12.6 | 0.2 | | |
| Van7-96-38 HLY0102- | Abyssal | SWIR | Lherzolite | 5 | 9 | 116 | 27 | 1337 | 306 | 2 | 1 | 15 | 1 |
| 40-81 | Abyssal | Gakkel | Harzburgite | 1 | 4 | 99 | 10 | 1133 | 117 | 1.4 | 0.1 | | |
| PS59-235-17 | Abyssal | Gakkel | Lherzolite | 3 | 13 | 145 | 18 | 1664 | 209 | 3.1 | 0.8 | | |
| 7TOW-57-4 BMRG08- | Abyssal | Tonga Trench | Harzburgite | 1 | 6 | 91 | 8 | 1043 | 96 | <0.1 | | | |
| 98-2-1 NOVA-88- | Abyssal | Tonga Trench | Harzburgite | 2 | 4 | 77 | 10 | 885 | 120 | <0.1 | | | |
| A1 | Abyssal | Tonga Trench | Harzburgite | 1 | 2 | 116 | 13 | 1335 | 154 | < 0.1 | | | |
| LS-33 | Xenolith | Pali Aike | Gt Lherz | 2 | 6 | 216 | 18 | 2488 | 213 | 25.9 | 0.6 | 4.3 | 0.5 |
| TMO | Xenolith | Pali Aike | Gt-Sp Lherz | 2 | 6 | 287 | 9 | 3304 | 103 | 16.0 | 0.6 | 9 | 2 |
| SAV-AS1 | Xenolith | Spitsbergen | Lherzolite | 2 | 7 | 186 | 5 | 2133 | 53 | 4.21 | 0.07 | | |
| SAV-AS2 | Xenolith | Spitsbergen | Lherzolite | 2 | 3 | 137 | 10 | 1576 | 119 | 1.9 | 0.1 | | |
| SA-3-9 | Xenolith | Samoa | Harzburgite | 1 | 2 | 99 | 9 | 1136 | 104 | 10.8 | 0.3 | | |
| SAV-1-28 | Xenolith | Samoa | Harzburgite | 1 | 3 | 118 | 11 | 1355 | 126 | 17.2 | 0.8 | | |

| 3923J01 | Orogenic | Josephine | Harzburgite | 1 | 1 | 168 | 15 | 1934 | 168 | < 0.1 | | | |
|--|--|--|---|--|---|--|--|--|---|--|---|---------------------|--------------------------|
| 3924J08 | Orogenic | Josephine | Harzburgite | 2 | 5 | 216 | 19 | 2487 | 220 | < 0.1 | | | |
| 3925G01 | Orogenic | Josephine | Harzburgite | 1 | 1 | 306 | 27 | 3516 | 305 | < 0.1 | | | |
| JP08PS01 | Orogenic | Josephine | Harzburgite | 3 | 6 | 265 | 38 | 3048 | 440 | < 0.1 | | | |
| | | | Clinopyroxene | | | | | | | | | | |
| PS86-6-38 | Abyssal | SWIR | Lherzolite | 1 | 2 | 459 | 10 | 5594 | 118 | 10.3 | 0.3 | | |
| Van7-85-30 | Abyssal | SWIR | Harzburgite | 1 | 1 | 793 | 69 | 9676 | 839 | 0.5 | 0.1 | | |
| Van7-85-42 | Abyssal | SWIR | Lherzolite | 1 | 2 | 429 | 38 | 5229 | 463 | 0.7 | 0.1 | | |
| Van7-85-47 | Abyssal | SWIR | Lherzolite | 2 | 2 | 415 | 16 | 5059 | 197 | 1.3 | 0.4 | | |
| Van7-85-49 | Abyssal | SWIR | Lherzolite | 2 | 4 | 398 | 72 | 4855 | 881 | 3.1 | 0.2 | | |
| Van7-86-27 | Abyssal | SWIR | Lherzolite | 1 | 1 | 748 | 65 | 9124 | 792 | 0.1 | 0.0 | 1.1 | 0.2 |
| Van7-96- | | | | | | | | | | | | | |
| 09V | Abyssal | SWIR | Pyroxenite Vein | 6 | 14 | 59 | 19 | 716 | 237 | 18.5 | 2.5 | 5.2 | 3.5 |
| Van7-96- 16V | Abyssal | SWIR | Pyroxenite Vein | 1 | 1 | 644 | 135 | 7856 | 1643 | 4.1 | 2.8 | 14.8 | 7.5 |
| Van7-96- | Abyssai | SWIK | i yioxeinte vein | 1 | 1 | 044 | 133 | 7050 | 1075 | 7.1 | 2.0 | 17.0 | 1.5 |
| 18V | Abyssal | SWIR | Pyx Vn in Perid | 1 | 2 | 550 | 7 | 6707 | 82 | 23.6 | 0.9 | 6.6 | 0.6 |
| Van7-96- | | CHUP | 11 /D 17 | 2 | _ | 40.4 | 40 | 5908 | 40.4 | 43.9 | 8.4 | 25.5 | 1.0 |
| 013.6 | | | | | | | | 5000 | 494 | 449 | V /I | 25.5 | 1.2 |
| 21M Van 7-96- | Abyssal | SWIR | Harz w/ Pyx Vn | 2 | 5 | 484 | 40 | 3700 | | 13.7 | 0.4 | | |
| 21M Van7-96- 21V | | | · | | | 401 | 283 | 4891 | 3446 | 34.1 | 30.3 | 28.7 | |
| Van7-96- | Abyssal Abyssal | SWIR SWIR SWIR | Pyx Vn in Harz Lherzolite | 3 2 | 5 5 4 | | | | | | | 28.7 14.2 | 3.8 0.6 |
| Van7-96- 21V | Abyssal | SWIR | Pyx Vn in Harz | 3 | 5 | 401 | 283 | 4891 | 3446 | 34.1 | 30.3 | | 3.8 |
| Van7-96- 21V Van7-96-25 | Abyssal Abyssal | SWIR SWIR | Pyx Vn in Harz Lherzolite | 3 2 | 5 4 | 401 458 | 283 33 | 4891 5591 | 3446 397 | 34.1 18.5 | 30.3 4.3 | 14.2 | 3.8 0.6 |
| Van7-96- 21V Van7-96-25 Van7-96-28 | Abyssal Abyssal Abyssal | SWIR SWIR SWIR | Pyx Vn in Harz Lherzolite Lherzolite | 3 2 3 | 5 4 6 | 401 458 613 | 283 33 35 | 4891 5591 7471 | 3446 397 431 | 34.1 18.5 28.1 | 30.3 4.3 7.0 | 14.2 14.7 | 3.8 0.6 1.5 |
| Van7-96- 21V Van7-96-25 Van7-96-28 Van7-96-35 | Abyssal Abyssal Abyssal | SWIR SWIR SWIR SWIR | Pyx Vn in Harz Lherzolite Lherzolite Lherzolite | 3 2 3 4 | 5 4 6 8 | 401 458 613 413 | 283 33 35 38 | 4891 5591 7471 5038 | 3446 397 431 458 | 34.1 18.5 28.1 66.2 | 30.3 4.3 7.0 9.7 | 14.2 14.7 | 3.8 0.6 1.5 |
| Van7-96- 21V Van7-96-25 Van7-96-35 Van7-96-38 | Abyssal Abyssal Abyssal Abyssal | SWIR SWIR SWIR SWIR SWIR | Pyx Vn in Harz Lherzolite Lherzolite Lherzolite Lherzolite | 3 2 3 4 1 | 5 4 6 8 1 | 401 458 613 413 665 | 283 33 35 38 58 | 4891 5591 7471 5038 8106 | 3446 397 431 458 703 | 34.1 18.5 28.1 66.2 3.3 | 30.3 4.3 7.0 9.7 0.1 | 14.2 14.7 | 3.8 0.6 1.5 |
| Van7-96- 21V Van7-96-25 Van7-96-28 Van7-96-35 Van7-96-38 PS59-235-17 | Abyssal Abyssal Abyssal Abyssal Abyssal | SWIR SWIR SWIR SWIR SWIR Gakkel | Pyx Vn in Harz Lherzolite Lherzolite Lherzolite Lherzolite Lherzolite | 3 2 3 4 1 | 5 4 6 8 1 5 | 401 458 613 413 665 362 | 283 33 35 38 58 9 | 4891 5591 7471 5038 8106 4418 | 3446 397 431 458 703 115 | 34.1 18.5 28.1 66.2 3.3 10.1 | 30.3 4.3 7.0 9.7 0.1 2.4 | 14.2 14.7 | 3.8 0.6 1.5 |
| Van7-96- 21V Van7-96-25 Van7-96-28 Van7-96-35 Van7-96-38 PS59-235-17 7TOW-57-4 | Abyssal Abyssal Abyssal Abyssal Abyssal Abyssal | SWIR SWIR SWIR SWIR SWIR Gakkel Tonga Trench | Pyx Vn in Harz Lherzolite Lherzolite Lherzolite Lherzolite Lherzolite Harzburgite | 3 2 3 4 1 1 | 5 4 6 8 1 5 | 401 458 613 413 665 362 254 | 283 33 35 38 58 9 28 | 4891 5591 7471 5038 8106 4418 3094 | 3446 397 431 458 703 115 345 | 34.1 18.5 28.1 66.2 3.3 10.1 0.3 | 30.3 4.3 7.0 9.7 0.1 2.4 0.1 | 14.2 14.7 7.2 | 3.8 0.6 1.5 0.9 |
| Van7-96- 21V Van7-96-25 Van7-96-28 Van7-96-35 Van7-96-38 PS59-235-17 7TOW-57-4 LS-33 | Abyssal Abyssal Abyssal Abyssal Abyssal Abyssal Xenolith | SWIR SWIR SWIR SWIR SWIR Gakkel Tonga Trench Pali Aike | Pyx Vn in Harz Lherzolite Lherzolite Lherzolite Lherzolite Lherzolite Harzburgite Gt Lherz | 3 2 3 4 1 1 1 2 | 5 4 6 8 1 5 2 8 | 401 458 613 413 665 362 254 458 | 283 33 35 38 58 9 28 63 | 4891 5591 7471 5038 8106 4418 3094 5587 | 3446 397 431 458 703 115 345 772 | 34.1 18.5 28.1 66.2 3.3 10.1 0.3 52.9 | 30.3 4.3 7.0 9.7 0.1 2.4 0.1 0.6 | 14.2 14.7 7.2 | 3.8 0.6 1.5 0.9 |
| Van7-96- 21V Van7-96-25 Van7-96-28 Van7-96-35 Van7-96-38 PS59-235-17 7TOW-57-4 LS-33 TMO | Abyssal Abyssal Abyssal Abyssal Abyssal Abyssal Xenolith | SWIR SWIR SWIR SWIR SWIR Gakkel Tonga Trench Pali Aike | Pyx Vn in Harz Lherzolite Lherzolite Lherzolite Lherzolite Lherzolite Harzburgite Gt Lherz Gt-Sp Lherz | 3 2 3 4 1 1 1 2 2 | 5 4 6 8 1 5 2 8 13 | 401 458 613 413 665 362 254 458 667 | 283 33 35 38 58 9 28 63 70 | 4891 5591 7471 5038 8106 4418 3094 5587 8132 | 3446 397 431 458 703 115 345 772 853 | 34.1 18.5 28.1 66.2 3.3 10.1 0.3 52.9 47.4 | 30.3 4.3 7.0 9.7 0.1 2.4 0.1 0.6 2.7 | 14.2 14.7 7.2 | 3.8 0.6 1.5 0.9 |
| Van7-96- 21V Van7-96-25 Van7-96-28 Van7-96-35 Van7-96-38 PS59-235-17 7TOW-57-4 LS-33 TMO SAV-AS1 | Abyssal Abyssal Abyssal Abyssal Abyssal Abyssal Xenolith Xenolith | SWIR SWIR SWIR SWIR SWIR Gakkel Tonga Trench Pali Aike Pali Aike Spitsbergen | Pyx Vn in Harz Lherzolite Lherzolite Lherzolite Lherzolite Lherzolite Harzburgite Gt Lherz Gt-Sp Lherz Lherzolite | 3 2 3 4 1 1 1 2 2 2 | 5 4 6 8 1 5 2 8 13 4 | 401 458 613 413 665 362 254 458 667 350 | 283 33 35 38 58 9 28 63 70 | 4891 5591 7471 5038 8106 4418 3094 5587 8132 4270 | 3446 397 431 458 703 115 345 772 853 119 | 34.1 18.5 28.1 66.2 3.3 10.1 0.3 52.9 47.4 13.3 | 30.3 4.3 7.0 9.7 0.1 2.4 0.1 0.6 2.7 1.0 | 14.2 14.7 7.2 | 3.8 0.6 1.5 0.9 |

⁽a) Results are reported as the average and standard deviation of all points analyzed for each mineral phase in a sample. Numbers in grey italics are samples that are moderately to highly altered.

⁽c) Empty values correspond to grains for which P was not measured, as P was only analyzed for the last group of grains.



⁽b) Detection limit for F is 0.01 ppm in olivine, 0.1 ppm in Opx and Cpx.

Table 3: Mineral water concentrations in the model upper mantle^a

| | Ві | ulk | Oliv | /ine | 0 | рх | С | рх | |
|--------------------------------|------------------|------|--------|------------|------------------|------|--------|------|--|
| Concentration (ppm) | H_2O | H/Si | H_2O | H/Si | H ₂ O | H/Si | H_2O | H/Si | |
| Minimum estimate | 50 ^b | 626 | 8 | 132 | 73 | 844 | 191 | 2329 | |
| Maximum estimate | 200 ^b | 2505 | 32 | 527 | 294 | 3377 | 764 | 9316 | |
| Mineral Mode ^c | | | 57 | ' % | 28 | 3% | 13 | 3% | |
| Conversion Factor ^d | 1 | 3 | 1 | 6 | 1 | 1 | 1 | 2 | |

- (a) Mineral water concentrations determined from the bulk upper mantle water concentration, assuming D^{OI/Opx}=0.11 (experimental average) and D^{Cpx/Opx}=2.6 (xenolith average). See Figs. 2 & 6 for references for these partition coefficient datasets. Spinel is assumed to contain negligible amounts of water.
- (b) Upper mantle water estimate from Hirschmann, 2006.
- (c) Mineral modes for model upper mantle from Workman & Hart, 2005.
- (d) Conversion factor between ppm H₂O and ppm H/Si.

Table 4: Trace element concentrations in Cpx and Opx.

| Sample | Туре | Location | Р | K | Sc | Ti | Cr | Sr | Y | Zr | Nb | Ва | La | Се | Nd | Sm | Eu | Gd | Dy | Er | Yb | Hf | Data Source ^a |
|---------------|----------|-------------|----|----|-------|--------|------|--------|-------|-------|-------|-------|--------|--------|-------|-------|-------|-------|-------|-------|-------|-------|--------------------------|
| Clinopyroxene | | | | | | | | | | | | | | | | | | | | | | | |
| PS86-6-38 | Abyssal | SWIR | | | | 2412 | 4581 | 6.28 | 18.90 | 8.67 | 0.002 | | 0.037 | 0.569 | 2.385 | 1.338 | 0.587 | 2.170 | 2.843 | 1.584 | 1.524 | 0.456 | Warren, 2007 |
| Van7-85-30 | Abyssal | SWIR | | | | 1291 | 6284 | 0.75 | 13.69 | 1.39 | | | 0.030 | 0.030 | 0.287 | 0.397 | 0.213 | 0.999 | 1.681 | 1.059 | 1.014 | | Warren, 2007 |
| Van7-85-42 | Abyssal | SWIR | | | | 1220 | 5863 | 0.75 | 12.52 | 1.01 | 0.004 | | 0.016 | 0.023 | 0.257 | 0.401 | 0.203 | 0.994 | 1.708 | 1.128 | 1.077 | 0.096 | Warren, 2007 |
| Van7-85-47 | Abyssal | SWIR | | | | 1011 | 4947 | 0.38 | 12.23 | 0.45 | 0.004 | | 0.007 | 0.015 | 0.270 | 0.385 | 0.185 | 1.010 | 1.729 | 1.141 | 1.077 | 0.086 | Warren, 2007 |
| Van7-85-49 | Abyssal | SWIR | | | | 1001 | 5151 | 1.55 | 13.46 | 0.88 | 0.003 | | 0.013 | 0.025 | 0.283 | 0.427 | 0.211 | 1.189 | 1.838 | 1.161 | 1.150 | 0.079 | Warren, 2007 |
| Van7-86-27 | Abyssal | SWIR | | | | 879 | 4001 | 0.81 | 7.49 | 0.48 | | 0.218 | 0.005 | 0.013 | 0.144 | 0.305 | 0.142 | 0.707 | 1.371 | 0.860 | 0.859 | | Warren, 2007 |
| Van7-96-09V | Abyssal | SWIR | 32 | 11 | 54 | 2162 | 4208 | 10.13 | 19.89 | 15.04 | 0.087 | 0.028 | 0.258 | 1.562 | 3.235 | 1.379 | 0.562 | 2.204 | 3.165 | 2.133 | 2.079 | 0.795 | This study |
| Van7-96-16V | Abyssal | SWIR | | | | 4091 | 3150 | 4.01 | 33.01 | 38.65 | | 0.101 | 0.072 | 1.095 | 3.490 | 1.848 | 0.603 | 2.117 | 3.850 | 2.448 | 2.138 | | Warren, 2007 |
| Van7-96-18M | Abyssal | SWIR | | | | 2952 | 4313 | 12.59 | 23.58 | 20.63 | | | 0.227 | 1.870 | 2.829 | 1.412 | 0.595 | | 2.817 | 1.750 | 1.597 | | Warren, 2007 |
| Van7-96-18V | Abyssal | SWIR | | | | 2700 | 2811 | 3.41 | 26.05 | 18.90 | | | 0.150 | 1.492 | 2.757 | 1.517 | 0.562 | | 3.816 | 2.490 | 2.312 | | Warren, 2007 |
| Van7-96-21M | Abyssal | SWIR | | | | 3356 | 4484 | 24.40 | 18.77 | 35.62 | | | 0.976 | 5.133 | 6.087 | 2.084 | 0.800 | 2.372 | 2.857 | 1.729 | 1.518 | | Warren, 2007 |
| Van7-96-21V | Abyssal | SWIR | | | | 4040 | 4495 | 21.65 | 20.47 | 45.74 | | | 1.037 | 5.277 | 6.205 | 2.245 | 0.779 | 2.366 | 2.996 | 1.729 | 1.623 | | Warren, 2007 |
| Van7-96-25 | Abyssal | SWIR | | | | 2538 | 5574 | 10.96 | 16.43 | 17.17 | | | 0.171 | 1.444 | 2.429 | 1.154 | 0.513 | 1.863 | 2.342 | 1.407 | 1.343 | | Warren, 2007 |
| Van7-96-28 | Abyssal | SWIR | | | | 2289 | 6529 | 76.14 | 11.31 | 18.08 | | | 1.070 | 4.005 | 3.517 | 1.248 | 0.485 | 1.575 | 1.687 | 0.916 | 0.927 | | Warren, 2007 |
| Van7-96-35 | Abyssal | SWIR | | | | 1798 | 8083 | 34.67 | 12.51 | 21.73 | | | 0.399 | 2.209 | 3.143 | 1.402 | 0.538 | 1.824 | 2.025 | 1.028 | 0.996 | | Warren, 2007 |
| Van7-96-38 | Abyssal | SWIR | | | | 2699 | 3948 | 11.81 | 20.04 | 15.25 | 0.003 | | 0.079 | 0.956 | 2.699 | 1.440 | 0.637 | 2.176 | 2.992 | 1.909 | 1.694 | 0.642 | Warren, 2007 |
| PS59-235-17 | Abyssal | Gakkel | 11 | 3 | 45 | 1390 | 7182 | 2.18 | 12.73 | 2.29 | 0.137 | 0.021 | 0.067 | 0.241 | 0.897 | 0.694 | 0.313 | 1.302 | 1.953 | 1.341 | 1.256 | 0.377 | This study |
| 7TOW-57-4 | Abyssal | Tonga SZ | 2 | 7 | 47 | 34 | 5158 | 0.54 | 0.32 | 0.12 | 0.143 | 0.017 | 0.012 | 0.017 | 0.007 | 0.002 | 0.002 | 0.008 | 0.017 | 0.056 | 0.141 | 0.003 | This study |
| NOVA-88-A1 | Abyssal | Tonga SZ | 1 | 4 | 48 | 59 | 5163 | 0.30 | 0.49 | 0.29 | 0.145 | 0.027 | 0.029 | 0.068 | 0.024 | 0.010 | 0.001 | 0.009 | 0.034 | 0.080 | 0.181 | 0.009 | This study |
| LS-33 | Xenolith | Pali Aike | 26 | 79 | 23 | 2147 | 8047 | 80.29 | 4.81 | 17.56 | 0.506 | 0.101 | 1.251 | 4.536 | 4.391 | 1.301 | 0.416 | 1.239 | 1.034 | 0.424 | 0.315 | 0.669 | This study |
| TMO | Xenolith | Pali Aike | 34 | 19 | 27 | 3134 | 6247 | 76.70 | 4.64 | 25.73 | 0.716 | 0.022 | 1.708 | 4.519 | 4.527 | 1.475 | 0.440 | 1.426 | 1.123 | 0.373 | 0.240 | 0.865 | This study |
| SAV-AS1 | Xenolith | Spitsbergen | 52 | 3 | 64 | 2496 | 4426 | 288.74 | 16.83 | 34.57 | 0.099 | 0.092 | 15.402 | 22.428 | 6.557 | 1.599 | 0.603 | 2.192 | 2.813 | 1.848 | 1.750 | 1.236 | This study |
| SAV-AS2 | Xenolith | Spitsbergen | 35 | 4 | 63 | 2164 | 4337 | 53.22 | 15.67 | 7.81 | 0.088 | 0.041 | 4.981 | 7.383 | 2.930 | 0.998 | 0.419 | 1.770 | 2.525 | 1.726 | 1.589 | 0.652 | This study |
| SA-3-9 | Xenolith | Samoa | | | 32.15 | 26.58 | 6612 | 0.2 | | 2.05 | | | 0.29 | 0.20 | 0.03 | 0.01 | 0.01 | | 0.03 | 0.07 | 0.13 | | Hauri & Hart, 1994 |
| SAV-1-28 | Xenolith | Samoa | | | 33.67 | 256.93 | 5903 | 158.8 | | 27.43 | | | 42.97 | 111.57 | 49.20 | 9.21 | 2.20 | | 3.62 | | 1.44 | | Hauri et al., 1993 |
| JP08PS01 | Orogenic | Josephine | 28 | 7 | 39 | 212 | 8579 | 0.44 | 1.37 | 0.10 | 0.128 | 0.044 | 0.014 | 0.012 | 0.002 | | | 0.059 | 0.131 | 0.129 | 0.246 | 0.014 | This study |

Orthopyroxene

| Van7-85-42 | Abyssal | SWIR | | | | | | | 1.87 | | 0.003 | | 0.002 | | 0.007 | 0.016 | 0.011 | 0.066 | 0.220 | 0.218 | 0.341 | 0.010 | Warren et al., 2009 |
|---------------|----------|-------|----|---|----|-----|------|------|------|------|-------|-------|-------|-------|-------|-------|-------|-------|-------|-------|-------|-------|---------------------|
| Van7-85-47 | Abyssal | SWIR | | | | | | | 1.82 | 0.01 | 0.003 | | | | 0.007 | 0.011 | 0.010 | 0.063 | 0.200 | 0.220 | 0.341 | 0.018 | Warren et al., 2009 |
| Van7-85-49 | Abyssal | SWIR | | | | | | 0.02 | 1.86 | | | | | | | 0.016 | 0.010 | 0.066 | 0.209 | 0.211 | 0.336 | 0.011 | Warren et al., 2009 |
| Van7-96-09V | Abyssal | SWIR | 30 | 3 | 25 | 696 | 1662 | 0.36 | 2.46 | 2.09 | 0.004 | 0.028 | 0.014 | 0.019 | 0.057 | 0.041 | 0.012 | 0.099 | 0.285 | 0.325 | 0.491 | 0.107 | This study |
| Van7-96-21Mat | Abyssal | SWIR | | | | | | 0.72 | 2.35 | 4.28 | 0.001 | | 0.019 | 0.102 | 0.169 | 0.087 | 0.038 | 0.162 | 0.309 | 0.271 | 0.389 | 0.156 | Warren et al., 2009 |
| Van7-96-25 | Abyssal | SWIR | 54 | 4 | 16 | 601 | 3606 | 0.37 | 1.07 | 1.15 | 0.009 | 0.023 | 0.048 | 0.021 | 0.032 | 0.020 | 0.006 | 0.051 | 0.126 | 0.135 | 0.234 | 0.051 | This study |
| Van7-96-28 | Abyssal | SWIR | | | | | | 1.65 | 1.41 | 1.65 | 0.013 | | 0.020 | 0.057 | 0.085 | 0.054 | 0.022 | 0.096 | 0.183 | 0.152 | 0.225 | 0.061 | Warren et al., 2009 |
| Van7-96-38 | Abyssal | SWIR | | | | | | 0.23 | 2.57 | 2.01 | | | | 0.018 | 0.067 | 0.054 | 0.026 | 0.128 | 0.309 | 0.279 | 0.408 | 0.115 | Warren et al., 2009 |
| SAV-1-28 | Xenolith | Samoa | | | | 7.4 | | 0.22 | | 2.2 | | | 0.13 | 0.19 | 0.33 | 0.09 | 0.04 | | 0.23 | 0.18 | 0.28 | | Hauri et al., 1993 |

⁽a) Data in this study collected by 6f SIMS at DTM; data from Warren (2007) collected by solution ICPMS at ISEI, Misasa and 3f SIMS at NENIMF, WHOI; data from Warren et al., 2009 collected by solution ICPMS at ISEI, Misasa.

Table 5: Water partition coefficients derived from mineral data.

| | Sample | Туре | Location | Lithology | D ^{OI/Opx} | D ^{OI/Cpx} | D ^{Cpx/Opx} |
|----------|---------------------------|--------------------|-----------------|---------------------------|---------------------|---------------------|----------------------|
| | PS86-6-38 | Abussal | CWID | l bay-alita | | | 0.7 |
| | Van7-85-30 | Abyssal | SWIR SWIR | Lherzolite | | | 2.7 2.7 |
| | Van7-85-42 | Abyssal | SWIR | Harzburgite Lherzolite | | | 2.7 2.9 |
| | Van7-85-47 | Abyssal | SWIR | Lherzolite | | | 2.9 2.6 |
| | Van7-85-47 Van7-85-49 | Abyssal | SWIR | Lherzolite | | | 2.0 |
| | Van7-95-49 Van7-96-09V | Abyssal | SWIR | Pyx Vn | | | 2.0 6.4 |
| | Van7-96-16V | Abyssal | SWIR | • | | | 1.7 |
| | Van7-96-18V | Abyssal | SWIR | Pyx Vn Pyx Vn in Perio | | | 25.2 |
| | Van7-96-21M | Abyssal Abyssal | SWIR | Harz w/ Pyx Vr | | | 3.3 |
| | Vai17-90-2 11VI | Abyssai | SWIK | Pyx Vn in | ı | | 3.3 |
| | Van7-96-21V | Abyssal | SWIR | Harz | | | 2.5 |
| | Van7-96-25 | Abyssal | SWIR | Lherzolite | | | 22.2 |
| | Van7-96-28 | Abyssal | SWIR | Lherzolite | | | 5.0 |
| | Van7-96-35 | Abyssal | SWIR | Lherzolite | | | 4.8 |
| | Van7-96-38 | Abyssal | SWIR | Lherzolite | | | 5.7 |
| | HLY0102-40- | | | | | | |
| | 81 | Abyssal | Gakkel | Harzburgite | 0.02 | | |
| | PS59-235-17 | Abyssal | Gakkel Tonga | Lherzolite | | | 2.5 |
| | 7TOW-57-4 | Abyssal | Trench | Harzburgite | 0.03 | 0.01 | 2.8 |
| | BMRG08-98- | , , | Tonga | | | | |
| | 2-1 | Abyssal | Trench | Harzburgite | 0.04 | | |
| | LS-33 | Xenolith | Pali Aike | Gt Lherz | 0.06 | 0.03 | 2.1 |
| | TMO | Xenolith | Pali Aike | Gt-Sp Lherz | 0.03 | 0.01 | 2.3 |
| | SAV-AS1 | Xenolith | Spitsbergen | Lherzolite | 0.02 | 0.01 | 1.9 |
| | SAV-AS2 | Xenolith | Spitsbergen | Lherzolite | 0.04 | 0.02 | 2.2 |
| | SA-3-9 | Xenolith | Samoa | Harzburgite | 0.04 | | |
| | 3923J01 | Orogenic | Josephine | Harzburgite | 0.06 | | |
| | 3924J08 | Orogenic | Josephine | Harzburgite | 0.03 | | |
| | 3925G01 | Orogenic | Josephine | Harzburgite | 0.03 | | |
| | JP08PS01 | Orogenic | Josephine | Harzburgite | 0.03 | 0.02 | 1.8 |
| | Average (exclud | ling Van7-96 | 3) | | 0.04 | 0.02 | 2.4 |
| | Standard deviati | - | -, | | 0.01 | | 0.4 |
| | N | | | | 12 | 6 | 11 |
| | | | | | | | |
| | | | | | | | |
| | | | | | | | |
| | | | | | | | |
| | | | | | | | |
| | | | | | | | |
| | | | | | | | |
| | | | | | | | |
| 4 | | | | | | | |
| | | | | | | | |
| | | | | | | | |
| | | | | | | | |

Table 6: Peridotite compositions and calculated variables^a

| 4 | | | | | Measu | ıred | | | | (| Calculat | ed | |
|---------------------------|-----------------|-----------|-------|------|-------|------|-------|------|------|----------|----------|----------|------------------------|
| | | Bulk | Spin | Срх | | | Modes | | | Oliv | Bulk | Bulk | Effective |
| Sample | Location | Al_2O_3 | Cr# | Ce | Oliv | Орх | Срх | Spin | Gt | H_2O^b | H_2O^c | Ce^{d} | Viscosity ^e |
| | | wt% | | ppm | | · | · | • | | ppm | ppm | ppm | Pas |
| PS86-6-38 | SWIR | 3.50 | 11.26 | 0.57 | 0.57 | 0.29 | 0.13 | 0.02 | | 19 | 118 | 0.077 | 1.2E+20 |
| Van7-85-42 | SWIR | 2.28 | 15.91 | 0.02 | 0.67 | 0.26 | 0.06 | 0.01 | | 16 | 75 | 0.002 | 1.4E+20 |
| Van7-85-47 | SWIR | 2.45 | 17.40 | 0.01 | 0.69 | 0.25 | 0.05 | 0.01 | | 17 | 72 | 0.001 | 1.3E+20 |
| Van7-85-49 | SWIR | 1.84 | 14.95 | 0.03 | 0.72 | 0.22 | 0.05 | 0.01 | | 22 | 81 | 0.002 | 9.9E+19 |
| Van7-96-09V | SWIR | 8.79 | 34.44 | 1.56 | 0.11 | 0.30 | 0.57 | 0.02 | | 1 | 36 | 0.904 | 2.5E+21 |
| Van7-96-18M | SWIR | 2.97 | 10.19 | 1.87 | | | | | | 4 | | | 7.7E+20 |
| Van7-96-18V | SWIR | 8.27 | 16.02 | 1.49 | | | | | | 2 | | | 2.5E+21 |
| Van7-96-21M | SWIR | 2.37 | 26.54 | 5.13 | 0.77 | 0.18 | 0.05 | 0.01 | | 16 | 62 | 0.273 | 1.4E+20 |
| Van7-96-21V | SWIR | 4.87 | 16.61 | 5.28 | 0.20 | 0.40 | 0.38 | 0.02 | | 18 | 220 | 2.080 | 1.3E+20 |
| Van7-96-25 | SWIR | 2.52 | 13.75 | 1.44 | 0.66 | 0.26 | 0.07 | 0.01 | | 2 | 38 | 0.111 | 2.5E+21 |
| Van7-96-28 | SWIR | 2.42 | 32.33 | 4.00 | 0.77 | 0.17 | 0.05 | 0.01 | | 13 | 65 | 0.242 | 1.8E+20 |
| Van7-96-35 | SWIR | 1.42 | 23.96 | 2.21 | 0.71 | 0.17 | 0.11 | 0.02 | | 10 | 65 | 0.246 | 2.7E+20 |
| Van7-96-38 HLY0102-40- | SWIR | 4.10 | 11.50 | 0.96 | 0.64 | 0.24 | 0.10 | 0.02 | | 13 | 102 | 0.103 | 1.9E+20 |
| 81 | Gakkel | 0.98 | | | 0.68 | 0.30 | 0.00 | 0.01 | | 11 | 38 | | 2.3E+20 |
| PS59-235-17 | Gakkel Tonga | | | 0.24 | | | | | | 16 | | | 1.4E+20 |
| 7TOW-57-4 BMRG08-98- | Trench Tonga | 0.52 | | 0.02 | 0.80 | 0.18 | 0.01 | 0.00 | | 10 | 28 | 0.0003 | 2.5E+20 |
| 2-1 | Trench Tonga | 0.42 | 58.36 | | 0.85 | 0.14 | 0.00 | 0.01 | | 8 | 18 | | 3.1E+20 |
| NOVA-88-A1 | Trench | | | 0.07 | 0.79 | 0.20 | 0.00 | 0.01 | | 13 | 34 | 0.0006 | 1.9E+20 |
| LS-33 | Pali Aike | 3.43 | | 4.54 | 0.55 | 0.20 | 0.15 | | 0.10 | 24 | 125 | | 8.9E+19 |
| TMO | Pali Aike | 2.86 | | 4.52 | | | | | | 32 | | | 6.3E+19 |
| SAV-AS1 | Spitsbergen | | | 22 | | | | | | 20 | | | 1.1E+20 |
| SAV-AS2 | Spitsbergen | | | 7.38 | | | | | | 15 | | | 1.5E+20 |
| SA-3-9 | Samoa | | 47.20 | 0.20 | 0.77 | 0.22 | 0.01 | 0.01 | | 11 | 31 | 0.003 | 2.3E+20 |

| SAV-1-28 | Samoa | 1.34 | 37.80 | 112 | 0.68 | 0.28 | 0.03 | 0.01 | 13 | 51 | 4.565 | 1.8E+20 |
|----------|-----------|------|-------|------|------|------|------|------|----|----|-------|---------|
| 3923J01 | Josephine | | | | | | | | 19 | | | 1.2E+20 |
| 3924J08 | Josephine | | | | | | | | 24 | | | 8.9E+19 |
| 3925G01 | Josephine | | | | | | | | 34 | | | 5.9E+19 |
| JP08PS01 | Josephine | | | 0.01 | | | | | 29 | | | 7.0E+19 |

^aCompositional data for SWIR samples from Warren et al. (2009) and Craddock et al. (2013); for Pali Aike from Stern et al. (1989, 1999); for Samoa from Hauri et al. (1993) and Hauri & Hart (1994).



^bCalculated olivine H₂O concentrations from Opx H₂O concentrations, assuming D_{Ol/Opx}=0.11.

^cSpinel and garnet are excluded from the bulk concentration calculation due to the very low abundance of water in these minerals, along with the low modal abundance of spinel.

^dBulk Ce concentrations are calculated from measured Cpx Ce concentrations and mineral modes, using the formulation in Workman and Hart (2005) and Ce mineral/melt partition coefficients from Kelemen et al. (2004).

^eEffective viscosity, calculated as a function of olivine water content, at a temperature of 1200°C, pressure of 0.5 GPa, and shear stress of 0.3 MPa. See section 5.9 for details.

Accep

Table 7: Parameters used for modeling trace elements.

| | Partition Coefficient | Oliv/Melt | Ref. | Opx/Melt | Ref. | Cpx/Melt | Ref. | Bulk/Melt | Ref. |
|---|------------------------------|---------------|------------------------------|-------------------------|----------|---------------------------|--------|--------------------------|-------|
| | Published values for pa | rtition coeff | icients | | | | | | |
| | | | | | | | | 0.007 - | |
| | D _{H2O} | 0.0014 | 1 | 0.018 | 1,2 | 0.010 | 1,2 | 0.009 | 1,3 |
| | | | | | | | | 0.012 - | |
| | D_Ce | 0.00001 | 4 | 0.003 | 4 | 0.0858 | 5 | 0.022 | 4,6 |
| | D_{H2O}/D_{Ce} | 140 | | 6 | | 0.1 | | 0.3 - 0.4 | |
| | | | | | | | | | |
| | Internally consistent v | alues for D | _{н2О} , ba : | sed on D ^{Opx} | /Melt =0 | .018, D ^{Ol/Opx} | =0.11, | and D ^{Cpx/Opx} | =2.6 |
| 4 | D _{H2O} | 0.002 | calc. | 0.018 | 1,2 | 0.047 | calc. | 0.012 | calc. |
| | D_{H2O}/D_{Ce} | 200 | | 6 | | 0.5 | | 0.6 - 1.0 | |
| | | | | | | | | | |
| | Modes | Olivine | Ref. | Орх | Ref. | Срх | Ref. | Spinel | Ref. |
| | Source modes | 0.57 | 6 | 0.28 | 6 | 0.13 | 6 | 0.02 | 6 |
| | Melt modes | -0.06 | 7 | 0.28 | 7 | 0.67 | 7 | 0.11 | 7 |

References:

1=Hauri et al., 2006

2=O'Leary et al., 2010, assuming pyroxene ^{IV}Al³⁺=0.04-0.07

3=Hirschmann, 2006

4=Kelemen et al., 2003

5=Hart & Dunn, 1993

6=Workman & Hart, 2005

7=Kinzler, 1997